

Precision magnetometry using Rb-atomic  
magnetometers and oscillating neutron  
Ramsey Method: Producing fake axion fields  
at the NARZISS beamline

**Master Thesis**  
at the Faculty of Science  
University of Bern

submitted by  
Ivan Calic

February 2022

Supervisor:  
Prof. Dr. Florian Piegsa

Albert Einstein Center for Fundamental Physics  
Laboratory for High Energy Physics

### **Abstract**

Characterization of new high precision magnetometers as a possible option for measuring magnetic fields from the human body. The aim was to verify the applicability of new optically pumped magnetometers (OPM) [1] with a Rubidium vapor cell from the company QuSpin [2] for performing magnetocardiogram MCG and/or magnetoencephalogram MEG.

A monochromatic neutron beam was driven through a modified Ramsey setup, where the neutrons were exposed not only to a static magnetic field  $B_0$  in the interaction zone, but to an additional oscillating field  $B_a(t)$  which should mimic the axion gluon coupling. The goal was to see whether the amplitude of the neutron count oscillations would completely disappear when reaching certain frequencies of the additional oscillating field and this goal was achieved.

## Acknowledgments

First, I would like to thank my supervisor Prof. Dr. Florian Piegsa for giving me the possibility and freedom to work on an own project, addressing the problems and finding solutions to them on my own. Also I want to thank the workshop and electronics workshop crew, namely Roger Hänni, Jan Christen, Lorenzo Meier, Camilla Tognina and Lino Risch. Big thanks also go to Ivo Schulthess, who was my main contact person during my master thesis. Rest of the Neutron group (Jacob, Estelle, Anastasio, Marc, Gjon, Phillip.) The second part of this work was performed at the NARZISS beamline of the Swiss Spallation Neutron Source SINQ at the Paul Scherrer Institute in Switzerland. I also want to acknowledge Dr. Christine Klauser for her help and answers concerning beamline. At this point I also want to thank my family and friends, who supported me during my whole studies.

# Contents

<b>1</b>	<b>Introduction</b>	<b>2</b>
1.1	Magnetic fields of the human body . . . . .	2
1.2	Optically pumped Rubidium magnetometers . . . . .	3
<b>2</b>	<b>Methods</b>	<b>10</b>
2.1	Characterization of the Rb-OPM . . . . .	10
2.1.1	Hardware . . . . .	10
2.1.2	Control and DAQ . . . . .	11
2.1.3	Background check . . . . .	12
2.1.4	Frequency response . . . . .	15
2.1.5	Amplitude Scan . . . . .	16
2.2	Mu metal shielding . . . . .	17
2.2.1	Magnetic shielding factor . . . . .	17
2.2.2	Internal coil characterization . . . . .	21
2.3	Radiofrequency (RF) shielding . . . . .	24
2.4	Additional measurements . . . . .	29
2.4.1	Stability measurements . . . . .	29
2.4.2	Simulating the heart beat . . . . .	34
<b>3</b>	<b>Results and discussion</b>	<b>36</b>
<b>4</b>	<b>Introduction</b>	<b>37</b>
4.1	Motivation: Axions and producing fake axion fields . . . . .	37
4.2	Resonance Measurements . . . . .	38
4.2.1	Rabi technique . . . . .	38
4.2.2	Ramsey Technique . . . . .	39
4.3	Ramsey scan with a time dependent $B_a$ field . . . . .	41
<b>5</b>	<b>Methods</b>	<b>44</b>
5.1	Preliminary measurements . . . . .	44
5.1.1	Preparation in our lab . . . . .	44
5.1.2	Beamline at NARZISS . . . . .	50
5.1.3	Test measurements at NARZISS . . . . .	51
5.2	Experimental procedure . . . . .	56



CONTENTS	1
----------	---

---

6 Results and discussion	62
--------------------------	----

Bibliography	65
--------------	----

# Chapter 1

## Introduction

### 1.1 Magnetic fields of the human body

The human body is a source of magnetic fields. For the production of those fields, two mechanisms are responsible.

Currents of sodium, potassium and chlorine ions, generated during signal transmission or contraction in nerves and muscles are the first mechanism. In other words, fields produced by naturally occurring electric currents in the body. Those currents flow through "volume conductors", the general mass of fluids and tissues of the body. These currents can either be fluctuating and producing AC magnetic fields or steady and producing DC magnetic fields [3].

The brain and the heart are organs which are well known to generate ion currents. Measuring the currents from the heart with electrodes on the skin, produces the electrocardiogram ECG. The magnetic field around the torso by the currents generated in the heart is, when measured, called a magnetocardiogram MCG. The brain's currents at the scalp produce the electroencephalogram EEG and its magnetic fields around the head is called the magnetoencephalogram MEG [3].

The blood is electrically neutral and has therefore no contribution to the electric and magnetic fields.

In contrast to these naturally occurring fields, the second mechanism in which magnetic fields can be produced is by magnetic material in the body. The materials can be either diamagnetic, paramagnetic or ferromagnetic and do not occur naturally in the body, but are contaminants. The most common contaminant involved is magnetite ( $\text{Fe}_3\text{O}_4$ ), which is soluble in the body and harmless [3].

The distinction between fluctuating and steady magnetic fields is made, because the background and the method of measurement is different in both cases. All organs in the body that consist of or contain muscle or nerve tissues, produce fluctuating magnetic fields. The fibers of the heart muscle depolarize synchronously in contrast to other muscles in the body. They produce the highest fluctuating magnetic fields. The peak is greater than 10 pT in ordinary subjects [3].

Concerning nerve tissues, the brain produces the highest magnetic fields. During sleep

the brain yields the largest fields, of a few hundred fT. Compared to the fields the heart fibers produce, measuring the brains magnetic fields is more challenging, since the fluctuating component of the background can be very strong.

Steady magnetic fields are produced by magnetite particles in the lungs and by steady currents from some organs. As a result of certain occupations of people, the amount of  $\text{Fe}_3\text{O}_4$  in the lung can be large. These particles produce remanent fields of one order of magnitude higher than the fields of the heart. Steady ion currents are caused under special circumstances of excitable tissues like injuries. The first magnetically seen and curious case is the magnetic field produced at the abdomen, due to an ion current generated as a reflex mechanism after drinking cold water [4].

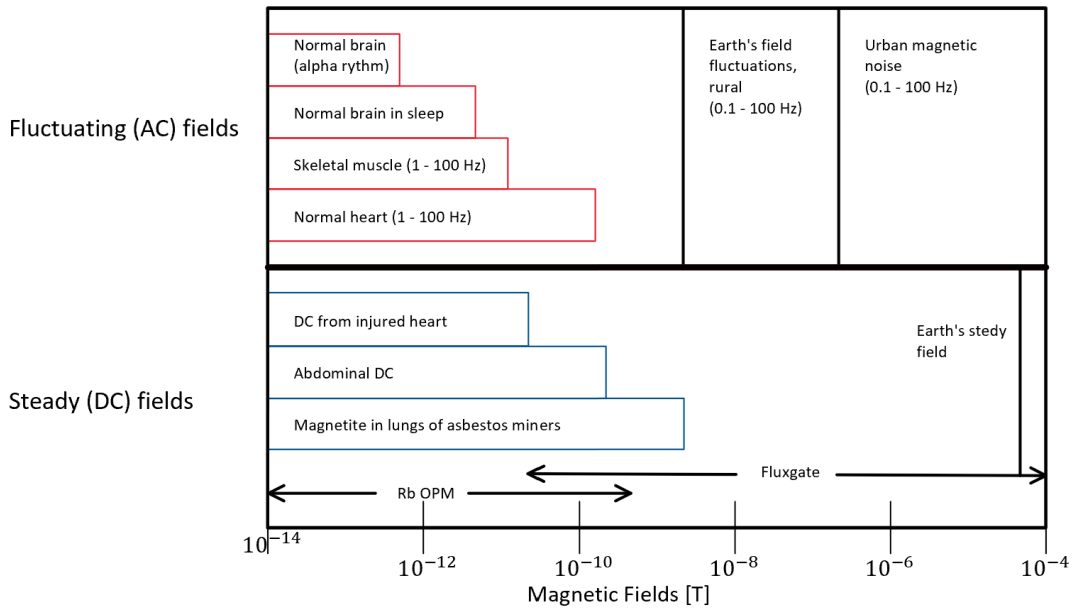


Figure 1.1: Magnitudes of different magnetic fields compared to the remanent fields (adapted from [3])

## 1.2 Optically pumped Rubidium magnetometers

To construct an optically pumped magnetometer as simple as possible, three components are needed. A laser or discharge lamp as a light source, high pressure vapor and a detection system, for example a photo diode.

Electromagnetic waves are emitted by the laser. This establishes a magnetically sensitive state in the vapor by transferring polarized light to it. This process of developing a magnetically sensitive state is referred to as optical pumping. Once this state is reached, the light is no longer absorbed by the polarized vapor. It now passes through the vapor and is detected at the photo diode as a change in voltage. By disrupting this optically pumped state with the presence of an ambient magnetic field, also the overall polarization

is reduced and therefore also the amount of transmitted light is reduced, since the vapour absorbs a part of the polarized light to reestablish the polarization. This leads to a change in the voltage of the photo diode, and this output varies as a function of the magnetic field.

The description just stated describes only the simplest setup for a optically pumped magnetometer. In more complicated setups two lasers may be used, one for the pumping, to induce the magnetically sensitive state (usually called the pump beam) and the second one for measuring the change in the intensity at the detector (usually called probe beam) [5].

When a light source transfers angular momentum to a sample so that all atoms from the sample occupy the same energy level, then it is called optical pumping. The total angular momentum  $\vec{F}$  in a weak magnetic field is the sum of the angular momentum of the nucleus  $\vec{I}$  and electron  $\vec{J}$ .

$$\vec{F} = \vec{I} + \vec{J} \quad (1.1)$$

The electron angular momentum further consists of an orbital momentum  $\vec{L}$  and a spin angular momentum  $\vec{S}$ .

$$\vec{J} = \vec{L} + \vec{S} \quad (1.2)$$

The nuclear angular momentum and the spin angular momentum of the electron are not a result of motion as in the classical mechanics. This form of angular momentum is rather intrinsic to the atom. One could interpret these forms of quantum angular momentum in terms of their observable effects. The total angular momentum ( $\vec{F}$ ) is associated with the total magnetic moment of the atom ( $\mu_F$ ),

$$\mu_F = \gamma \vec{F} \quad (1.3)$$

where  $\gamma$  is the gyromagnetic ration of the atom. For  $^{87}\text{Rb}$ ,  $\gamma$  has a value of approximately  $7 \text{ Hz nT}^{-1}$  [6]. If there is a magnetic field  $\vec{B}$ , this magnetic moment is associated with a potential energy  $V$

$$V = -\mu_F \vec{B} \quad (1.4)$$

These relations show the fundamental relationships between energy, angular momentum, magnetic moment and magnetic field. If for any reason the total angular momentum of the atom  $\vec{F}$  changes, also the magnetic moment  $\mu_F$  and potential energy  $E$  will change. So when the laser beam transfers angular momentum to the atom, the potential energy will change.

The outermost electron can exist in a number of discrete states. In order to change this state, energy has to either be absorbed or emitted. The interaction between the electron's orbital angular momentum and the spin angular momentum gives rise to the energy level difference which is called the fine structure splitting. These momenta define the energy levels and they can be described by the dimensionless quantum numbers  $S$  and  $L$ . For  $^{87}\text{Rb}$ , these quantum numbers can take values of:

- 0, 1, 2, 3, 4 for  $L$

- 1/2 for S

The quantum number relate to the magnitude of the momenta in the following way:

$$|\vec{S}| = \sqrt{S(S+1)}\hbar, \quad (1.5)$$

$$|\vec{L}| = \sqrt{L(L+1)}\hbar \quad (1.6)$$

The energy levels, due to the interaction of the orbital angular momentum and the spin angular momentum are found by taking integer steps in the following way:

$$|L - S| \leq J \leq L + S, \quad (1.7)$$

where  $J$  is the quantum number of the total angular momentum. The values, which  $J$  can take, define the allowed energy levels. The number of these states define the fine structure splitting. In the ground state, the orbital angular momentum  $L$  of  $^{87}\text{Rb}$  is zero. In the ground state therefore, only one value satisfies the Eq. (1.7)  $J = 1/2$ .

For the first excited state ( $L = 1$ ), two possible values for  $J$  are allowed ( $J = 1/2$  and  $J = 3/2$ ), which satisfy equation (1.7). The transitions from the ground state ( $L = 0$ ) to this two states are known by convention as the D1 and D2 transition respectively as shown in figure 1.2. By choosing the appropriate frequency of the laser light, as the energy  $E$  each photon carries is equal to its frequency  $\nu$  multiplied by Planck's constant  $h$

$$E = h\nu, \quad (1.8)$$

we can selectively choose which energy level the atom will occupy. For  $^{87}\text{Rb}$  a laser with a wavelength of 795 nm one can select only the D1 transition from  $L = 0$  to the  $L = 1$ ,  $J = 1/2$  state.

The fine structure can further be split by the interaction of the electron's total angular momentum  $\vec{J}$  and the nucleus' angular momentum  $\vec{I}$ . The dimensionless quantum number  $F$ , which characterizes the hyperfine splitting is familiar to Eq. (1.7), which is simply:

$$|I - J| \leq F \leq I + J \quad (1.9)$$

The dimensionless quantum number  $I$  has a value of 3/2 for  $^{87}\text{Rb}$  [7], due to the relative contribution of protons and neutrons in the nucleus. As mentioned above, when only implying a D1 transition,  $J$  will always have a value of 1/2. Therefore the values for  $F$  will be  $F = 1$  or  $F = 2$ . This is also represented in figure 1.2.

In the presence of a magnetic field, the hyperfine structure is split further into distinct energy levels. This is the Zeeman splitting. Since the direction of the laser beam is fix, we will restrict this discussion about the effect the laser has on the total angular momentum  $\vec{F}$  to only one axis. When restricting only on one axis, the Zeeman splitting becomes very simple. This is done by introducing a new dimensionless number  $m_f$ , which we convert by multiplying the reduced Planck's constant  $\hbar$  to represent the component of

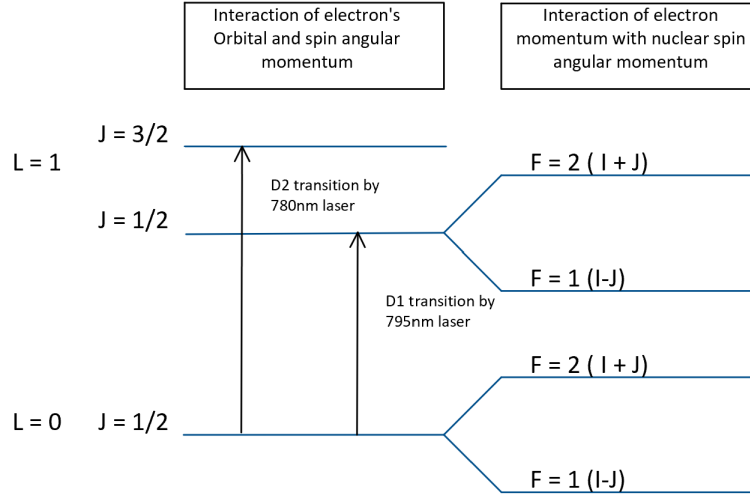


Figure 1.2: Sketch of the fine and hyperfine structure splitting of  $^{87}\text{Rb}$ . The left part shows the fine structure splitting, which results in the interaction between the electron's orbital and spin angular momentum. On the other side, the hyperfine structure splitting is a result of the interaction between the spin angular momentum of the nucleus  $I$  and the total angular momentum of the electron  $J$

the angular momentum along the laser beam axis

$$F_{\text{laser}} = \hbar m_f. \quad (1.10)$$

The values of  $m_f$  which are allowed are integer steps between  $-F$  and  $F$ . With this third splitting we can now describe the complete energy level diagram as in figure 1.3 for both, the ground state and the first excited state via the D1 transition of  $^{87}\text{Rb}$ . For both  $F = 1$  states, negative values of  $m_f$  have higher energy because of the different hyperfine states which are associated with the gyromagnetic ratios of opposite sign [6].

Since we now have the complete energy level diagram, we can start to describe how optical pumping is occurring by shining a laser light through the vapor cell. We have to consider two factors: the effect of the laser and the effect of the sample's spontaneously emitted energy. The governing rules of these effects are known as selection rules. The laser has two effects. The first effect is causing a D1 ( $\Delta L = 1$ ) transition, whereas the second is to increase the value of  $m_f$  (the value of the angular momentum along the beam axis). For alkali atoms, such as  $^{87}\text{Rb}$ , with a single outer shell electron  $m_f$  values will always increase when the laser light is positively circularly polarized. The polarization of the laser light is a manifestation for the angular momentum of the photon which is projected on the quantization axis. Thus when talking about the laser transferring polarization to the vapor, it transfers angular momentum. If the laser light was linearly polarized, an accumulation of angular momentum would not take place along the axis of the laser, but the D1 transfer would still happen.

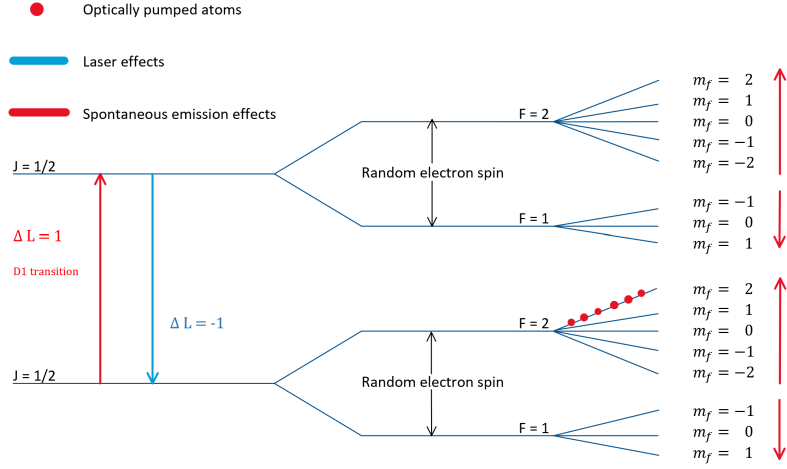


Figure 1.3: Optical pumping of  $^{87}\text{Rb}$ : The laser will always provide an increment in  $m_f$  and only if possible a D1 transition. This transition is only possible when  $m_f < 2$  (since the highest value for  $m_f$  in the  $L = 1$  state is 2). If the sample is in the  $L = 1$  state, it may emit spontaneously light at 795 nm as a reversed process of the D1 transition, but not necessarily changing  $m_f$ . This is caused by the fact, that emitted light has a equally distributed probability to emit light with  $m_f = 0, 1, -1$ . This results in an accumulation of the  $^{87}\text{Rb}$  atoms at the  $L = 0$  and  $m_f = 2$  state. Since there does not exist a  $m_f = 3$  state in  $L = 1$ , the laser can no longer induce a D1 transition.

The second factor we have to consider is the fact, that an excited atom can transit back to the ground state by emitting a photon. While the effect on  $L$  is reversed, the effect on  $m_f$  is not entirely reversed by the spontaneous emission. The reason for this is that spontaneous emitted light is equally likely to produce changes of  $\Delta m_f = 0, -1$  and 1. So the cases are equally distributed for retaining their polarization, losing an increment of polarization and gaining the same increment of  $m_f$ . When the atoms reach this state they become trapped there. Therefore, there is a net effect of the optical pumping on the value of  $m_f$  where it is pumped into its highest Zeeman sub level  $m_f = 2$  of the  $L = 0$  state. Another D1 transition to the  $L = 1$  state is no longer possible, since the laser also has to increase the value of the total atomic angular momentum along the beam axis  $m_f$ . But since the  $L = 1$  state has no energy level with  $m_f > 2$ , this transition is not allowed and the atoms are trapped in the  $L = 0$  and  $m_f = 2$  state. Therefore, if the atom is already in this state, the laser's light transfers no more energy to the sample and it is simply transmitted through the vapor. The vapor has become transparent to the laser light. This is the optical pumping as it is shown in Fig. 1.3.

When the atoms are pumped by laser into this steady transparent state, the vapor becomes highly polarized. According to Eq. (1.3), since many atoms occupy the same state, they produce collectively a strong net magnetization which is aligned along the axis of the laser beam.

This induced polarization is extremely sensitive to ambient magnetic fields. If the laser

beam was turned off when the vapor is in a polarized state and a static magnetic field with a component perpendicular to the net magnetization was present, then the magnetic moment of the atoms started to precesses with the Larmor frequency

$$\omega_L = \gamma B, \quad (1.11)$$

until the polarization of the vapor is eliminated by relaxation. With no laser beam, providing a circular polarized light, the precession would stop, since all atoms transited back to their ground state, where the vapor is no longer sensitive to magnetic fields. Turning the laser beam on will pump the atoms back to their sensitive state. In this state and with the presence of the magnetic field, the single atoms will again start to precess around the perpendicular component of the magnetic field until they lose their polarization due to relaxation. This happens to all the atoms but not all are at the same stage of this process of relaxation and excitation. Some may be in the pumping process while the others, which are already in the sensitive state, may be precessing or losing their sensitivity due to the precession or even to spontaneous emission. The net magnetization of the vapor, with the presence of a magnetic field, is deflected from the direction of the laser.

Every time, an atom has to be pumped back to its sensitive state, a part of the laser light no longer arrives at the photodetector, but is used to pump the atom. The stronger the magnetic field is, the more atoms are losing their sensitive state. Therefore, more laser light is used for the pumping and less light arrives at the photodetector. This causes a decrease in the transparency of the vapor which is sensed by the photodetector.

To explain how to measure the magnetic fields, imagine that there is no ambient magnetic field or that the OPM is in an absolute zero magnetic field environment. The net magnetization of the Rb vapor would stay aligned in the direction of the laser beam and no change in the transparency of the vapor would occur. Adding now a magnetic field perpendicular to the laser beam and sweeping the amplitude of the field from positive to negative values, the transparency of the vapor would change in a way that the maximum transparency would be at the amplitude close to zero. The output of the photodetector, as a function of the applied magnetic field, has the shape of an Lorentz absorption curve as it is shown in Fig. 1.4.

Having only the absorption curve as a signal is insufficient since it only gives the absolute value of the magnetic field with no sign. To get to the dispersion curve, which is the derivative of the absorption curve, an oscillating field at 1 kHz is applied. This oscillating field, also called modulation field, is applied by coils surrounding the vapor cell. A phase-sensitive lock-in amplifier is referenced to the frequency of the modulation field. The amplifier demodulates the signals of the photodetector, giving the dispersion curve as its output as it is shown in Fig. 1.4. This curve has its maximum slope at magnetic fields close to zero. In this region the signal is linear for changes of the transparency of the Rb vapor and therefore most precise. That is why it is called zero-field optically pumped magnetometers. The advantage of the dispersion curve is, that it also shows the sign of the magnetic fields, which is not the case for the absorption curve.



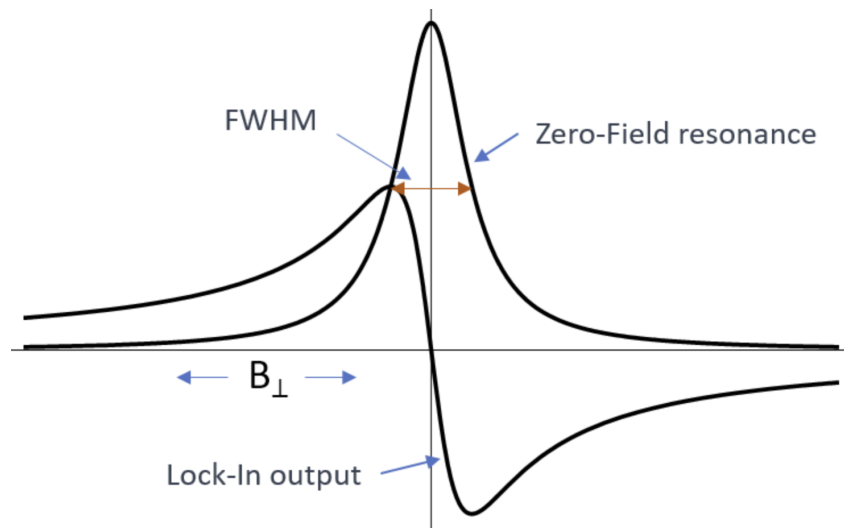


Figure 1.4: The absorption curve or the Zero-Field resonance would be the output of the photodetector if the magnetic field perpendicular to the laser beam was swept from positive to negative values. The width (FWHM) is typically 30 nT. The demodulated signal output of the lock-in amplifier gives the dispersion curve with the maximum slope at magnetic fields close to zero (Figure from [8]).

# Chapter 2

## Methods

### 2.1 Characterization of the Rb-OPM

#### 2.1.1 Hardware

For this work two Rb-OPM from the QuSpin company [2] were used. One set consist of one sensor cell and a QZFM electronics module as seen in Fig. 2.1. The electronics module has two outputs, one is a digital output, which besides to acquiring digital data is also used, to send further information about the sensors and to pilot the sensors. The second output is an analog DAQ. In comparison to the analog output, the digital data seen over USB has a built-in sixth-order low pass filter with a cut off frequency of 100 Hz and it is limited to a sample rate of 200 Hz.

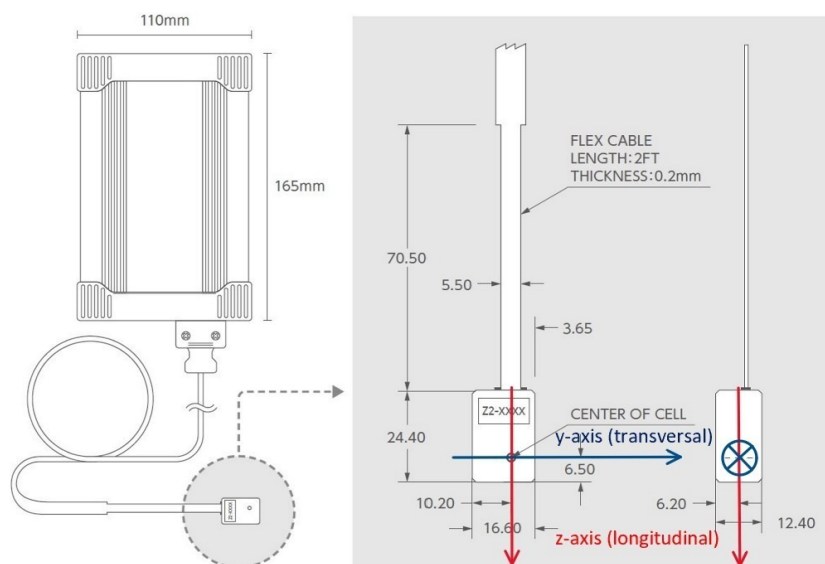


Figure 2.1: Schematic of the Rb-OPM hardware from QuSpins Website [2] with the coordinate system for the signals of the Rb sensor

Further there are ports for performing measurements with multiple magnetometer sets. Having more than one sensor in action, the electronics modules need to be in a master-slave configuration. The master electronics module distributes the modulation signal to the slave electronics modules, in order to minimize the interferences.

For the DAQ we used the analog readout from the electronics module. It has an 2.5 mm jack output with an jack to BNC converter included. The analog signals were then guided to a terminal block BNC-2110(model: BNC-2110, S/N: 1DFAC83) from National Instruments. This terminal block was connected to the National Instruments PCI-6289 Multifunction Data Acquisition Module (model: PXIe-1073, S/N: 30EA4B7) which is an analog to digital converter. After this conversion, the data was then directed to the neutron06 computer in the ExWi B64 (Cryolab).

### 2.1.2 Control and DAQ

Jacob Thorne, a member of the neutron group had already started to write a software for piloting the Rb sensors. The principle was simple. One has to send ASCII characters as commands to the electronics module and the module executes them. There is i.e. a command for the auto start process of the sensors. The module starts to boot and heats up the Rb-cells to their operating temperature. The starting procedure was always the same:

1. Turn the electronics module on and let the executable C program run.
2. The auto start process starts automatically and usually lasts for one or two minutes
3. The dual axis command was sent, otherwise only the z-axis is sensitive, while the y-axis is inactive.
4. Starting the zeroing calibration process with the field zero on command. The built in coils are now compensating the remanent fields.
5. When the field values stop fluctuating, the field zero off command was sent, to lock the compensation field inside of the Rb-sensors.
6. The last step was the calibration. After locking the compensation field, the calibration command finishes the starting process, where also the digital output values are shown in the piloting terminal.

To send a command during a running program, only one letter needs to be typed and confirmed by the return key. There is also a menu for all the commands, which will be displayed after typing "m" (for menu) and hitting the return key.

One could also have used the GUI that QuSpin provided. But the aim was to operate the sensors remote, which is not possible with the GUI.

Since we are reading out the analog output, also the converted digital data is showing only the voltage. Therefore this voltages had to be translated to magnetic fields with the conversion factor. The conversion factor at the normal gain mode (default setting) is 2.7

V/nT. The gain of the analog signal can be either increased or decreased by a factor of 3 and the conversion factor has to be changed accordingly.

For the DAQ a few programs were written.

One is continuously measuring, calculating the mean after every number of samples and plotting this mean values. This program was useful during the starting or zeroing processes, since it showed i.e. whether the magnetic fields were still fluctuating too much during the zeroing phase. Once these fluctuations decreased enough, the zeroing process was stopped and the compensation fields fixed. This program was only used to have a look at the values in real time and no data was written down.

For measuring longer periods, i.e. the stability measurements of the RF shielding in Sec. 2.3 the sampling rate was decreased drastically to 10 Hz. Also no mean was calculated from the data.

Shorter measurement at a time scale of around five seconds were recorded with a sampling rate of 10 kHz. The time could not be extended, since we had four channels to read out and in between each channel a 50  $\Omega$  resistor was placed to reduce the crosstalk between the channels. So with eight channels in use the NI device could not handle the amount of data for more than 50'000 samples (5 s measuring time).

### 2.1.3 Background check

The first measurement of the characterization had been the background scan to determine the noise for further measurements. Therefore, the Rb sensors were placed with their holdings (see Sec. 2.2, Fig. 2.9c) inside of the mu metal shielding (description of the used magnetic shielding can be found in Sec. 2.2). Figure 2.2 is showing the coordinate system for all the measurements performed with the Rb-OPMs.

For data acquisition, the analog output was used. With a sampling rate of 10 kHz and 50000 samples, each measurement lasted 5 s. Figure 2.3a shows the raw data of one single run. For a better understanding of the composition of the signals, a fast Fourier transformation was applied on the data. The Fourier transform, as seen in Fig. 2.4, indicates the contribution of each frequency to the total composition of the signal.

To increase the statistical accuracy and to get rid of random noise, the measurement was run 100 times and the mean of all Fourier transforms was calculated.

As mentioned in Sec. 2.1.1, the analog output has no low pass filter like the digital output. Especially with a high sampling rate (10000 Hz in our case) it is expected to pick up some noise at higher frequencies. To increase our signal to noise ratio (SNR), a Butterworth low pass filter of the sixth order :

$$G_6 = \frac{G_0}{\sqrt{1 + \left(\frac{\nu}{\nu_{\text{cut-off}}}\right)^{2 \cdot 6}}}, \quad (2.1)$$

where  $G_0$  is the DC gain,  $\nu_{\text{cut-off}}$  the cut-off frequency and the subscript "6" denotes the order of the filter, was implemented with a cut off frequency at 100 Hz. Figures 2.3b, 2.4 and 2.5 show for example the suppression of the high 200 Hz signal.

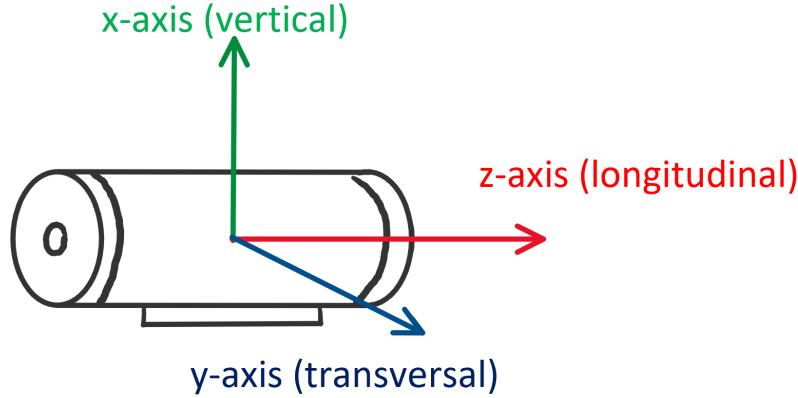


Figure 2.2: Schematic of the coordinate system. The Rb sensor has two active axis, the Y axis and Z axis, which is also visible in Fig. 2.1.

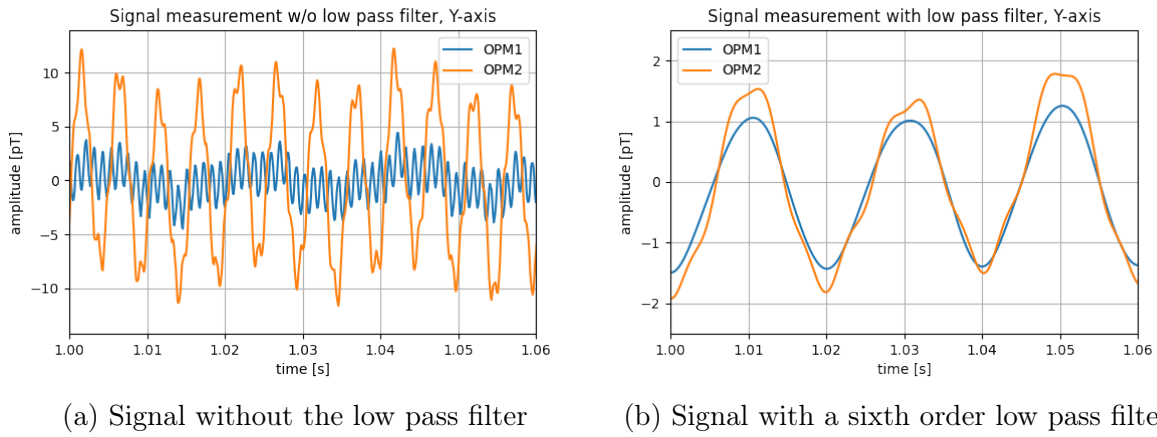


Figure 2.3: Background signal measured with the Rb sensors in the time domain. The signal of the first sensor is shown in blue and the signal from the second sensor in orange.

In the first Fig. 2.3, the signals of the Y axis (coordinate system in Fig. 2.2) in the time domain are shown. The left plot (Fig. 2.3a) is showing the signal from both sensors without the low pass filter. A big difference in the amplitudes is visible between the first and second sensor, whereas there is almost no difference in amplitude in the right plot in Fig. 2.3b. Looking at the left plot in Fig. 2.4, the peak for the second sensor at 200 Hz in the frequency domain is much higher than the one for the first sensor, which also explains the difference in amplitude in Fig. 2.3a.

Focusing now on the Fig. 2.4 and Fig. 2.5, which are the signals from both sensors separately plotted for each axis in the frequency domain. Comparing both axis, the Y axis and the Z axis, and focusing at the remanent fields of 16.8 Hz, which comes from the Swiss Federal Railways, there is one thing standing out. In Y direction (transversal direction) the 16.8 Hz is completely missing, whereas in Z direction the peak is clearly

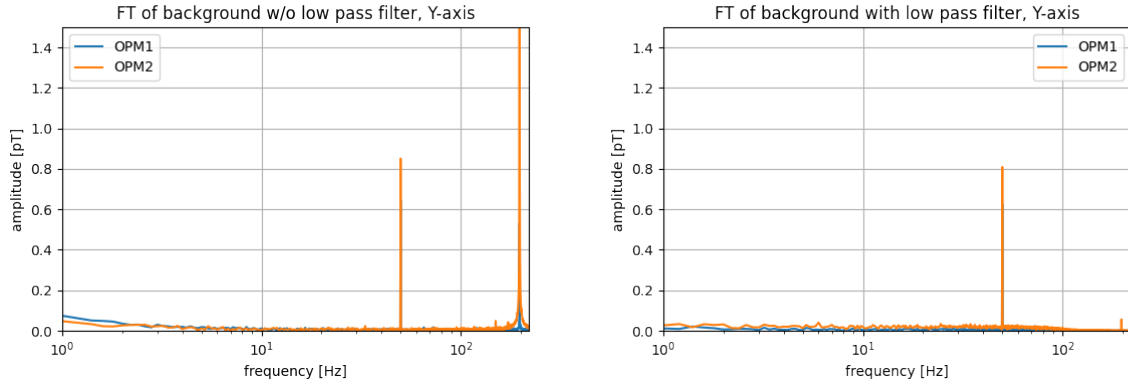


Figure 2.4: Spectrum of the background field, measured with the Rb sensors in Y direction in the frequency domain. On the left side, the FFT of the raw data is shown, whereas on the right side after processing the data through a low pass filter.

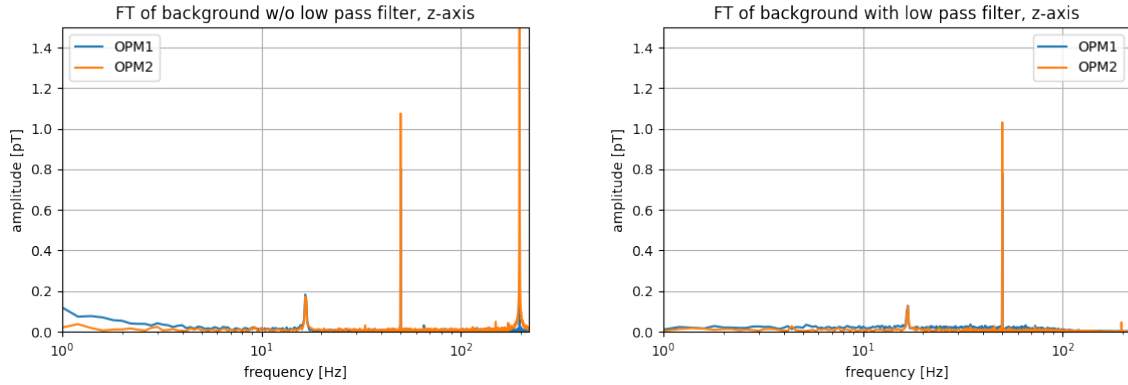


Figure 2.5: Spectrum of the background field, measured with the Rb sensors in Z direction in the frequency domain. Like in the upper figure 2.4 on the left side, the FFT of the raw data is shown, whereas on the right side after processing the data through a low pass filter.

visible. The reason of this could be that since the magnetic shielding has the best shielding factor in the transversal and vertical direction, it also shields this frequency better. The two bigger holes at both ends, used as openings to lead i.e. sensors inside of the shielding, may decrease the shielding factor (see Sec. 2.2.1) and therefore still guide some remanent fields through the axial holes.

Also at the 50 Hz frequency, which is the frequency of domestic powerlines, has a high contribution in both axis. As already seen in the 16.8 Hz signal, the Z axis shows a higher contribution of this noise source.

To dampen those signals at lower frequencies, additional shielding layers had to be installed. Such a radiofrequency (RF) shielding has been designed and installed. More about the RF shielding can be found in section 2.3.

### 2.1.4 Frequency response

The QuSpin QZFM Gen. 2 data sheet states a bandwidth of 135 Hz [2]. To check this information, the Rb-Sensors were placed with its holders, as it can be seen in section 2.2 in figure 2.9c, inside of the mu metal shielding. A waveform generator (WFG, Keysight, model: 33600A, S/N: MY59000421) was used to produce a sinusoidal signal and was connected via a resistor to the internal coils of the Twinleaf's MS-2 [9] mu metal shielding, which is described also in Sec. 2.2. Scanning the frequencies between 0.1 to 280 Hz, the fitted amplitudes of each measurement were plotted.

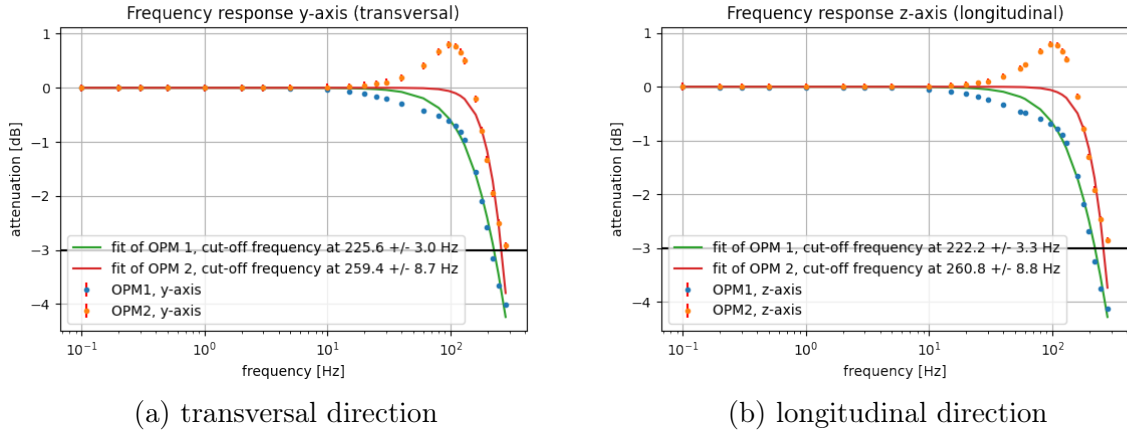


Figure 2.6: Frequency response of the Rb-OPM in both directions

Figure 2.6 is showing the attenuation of the signal over the frequency, with a limit of -3 dB showing the sensitivity. The attenuation was calculated with:

$$A(\nu) = 20 \cdot \log_{10} \left( \frac{a(\nu)}{a_0} \right), \quad (2.2)$$

where  $a(\nu)$  is the amplitude of a certain frequency and  $a_0$  the first measurement's amplitude at 0.1 Hz.

Figure 2.6 shows a strange behavior for the second sensor (OPM-2) for both directions when approaching 100 Hz, resulting in a bump at this frequency. The sensors could have picked up some additional contribution in the amplitude near this frequency, coming from the background signal at 50 Hz (Sec. 2.1.3) which is not enough suppressed from the magnetic shield. An increase in the result of the frequency scan at a frequency of 50 Hz is not visible, because it was avoided to induce oscillating fields near those known noise signal's frequencies (16.8 Hz and 50 Hz) and at their multiples. But it is possible, although it was tried to avoid, that the sensors picked up additional amplitude from the multiple of these frequencies.

Another explanation could be, that the induced oscillating magnetic fields were not in the direction of the active axis from the Rb-OPMs, which could also lead to this strange behavior and the bump at 100 Hz.

As mentioned in the beginning of this section, the data sheet stated a bandwidth of 135 Hz. The -3 dB cut-off frequency for both sensors and for both axis is above 200 Hz. Figure 2.6 shows also that the second sensor OPM 2 has a bandwidth of around 260 Hz, which is almost double the stated bandwidth of the data sheet.

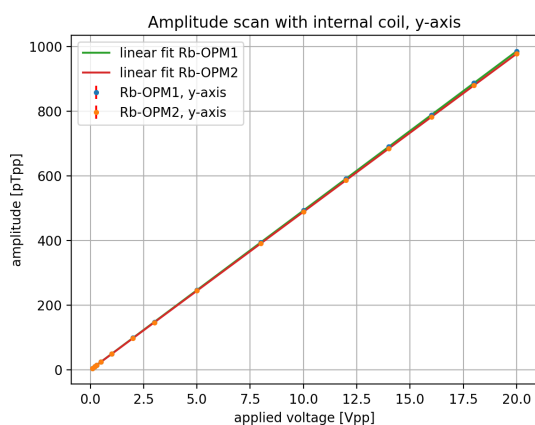
### 2.1.5 Amplitude Scan

To ensure the precision of the Rb sensors further, an amplitude scan was performed. This shows, whether the detection of the fields is linear in a certain regime. The QuSpin company states on their website, that the sensors should behave linear to a reference of 50 Hz signal field up to a 3 nTpp magnetic field. The interesting scale for our needs was the range of a few hundred of pT, so we expect the amplitude to behave linear.

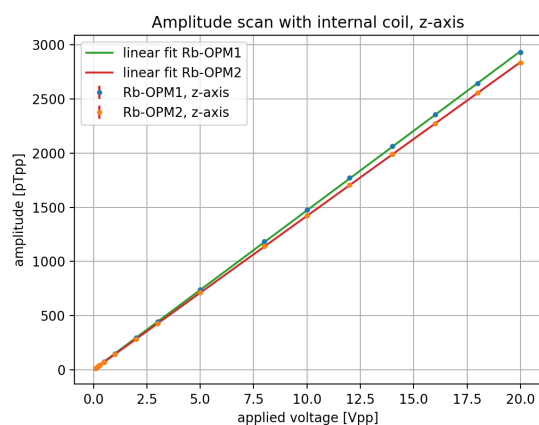
The Rb sensors were placed with a separation of 5 mm to each other on their holder and fixed inside the shielding. The signals were generated with a WFG and lead through a 10 k $\Omega$  resistor to the internal coil interface of Twinleaf's MS-2. The settings for the signal were:

- Frequency: 1 Hz
- Amplitude: from 0.1 Vpp to 20 Vpp in 15 steps
- Phase: No phase
- Offset: No offset

Firstly the amplitude scan was performed for the Y axis, then it was repeated for the Z axis as well. The signals were processed with a Python script to read out the amplitude of the signal.



(a) Amplitude scan of the sensor's Y axis



(b) Amplitude scan of the sensor's Z axis

Figure 2.7: Amplitude scan of both directions



For both axis, the amplitude of the measured magnetic fields rises linearly with the applied voltage, as seen in Fig. 2.7. The only difference between the Y axis and the Z axis is, that in Z direction the amplitudes drift apart at higher amplitudes, resulting in small differences for the slopes in the linear fits. This comes from the position of the Rb sensors in their holdings. The position can be varied, but only in Z direction. The Position in the Y direction is fixed, and therefore the sensors do not experience different fields in this direction since they have the same position in Y direction.

Overall, the sensors seem to behave linear for fields not only at our needed regime of below 300 pT, which was aimed to show, but also below 3 nT, which is also stated by the company [2].

## 2.2 Mu metal shielding

In Sec. 1.2 the requirement of low magnetic fields for operating the Rb OPMs was discussed. To enable measuring at such low fields, a proper shielding is mandatory.

In order to reach remanent fields at the pico Tesla or even femto Tesla scale, multiple layers of mu metal are necessary. The company Twinleaf provides such shieldings and ordered their MS-2 model [9]. The MS-2 does not only provide four layers of mu metal providing a shielding factor of  $10^6$  as they state it on their webpage. It has also inside of the first layer a coil network, which can be operated via the interface on the outside. One can apply homogeneous fields, field gradients and even gradients of the second order in one direction.

The dimensions of the MS-2 are shown in Fig. 2.8. The internal stage made of Polyoxymethylene (POM), which is not a source for interferences in the magnetic fields, with a breadboard hole pattern can be used for the positioning of the sensors. Since we wanted to use the internal coils for the characterization of the Rb OPMs, it would be necessary to have the sensors in the center of the coils to have the homogeneity of the fields. Therefore a holder for the Rb Sensors had to be designed, as shown in Fig. 2.9 to position them in the center of the shielding and internal coils.

As the internal stage, the holder is made out of POM.

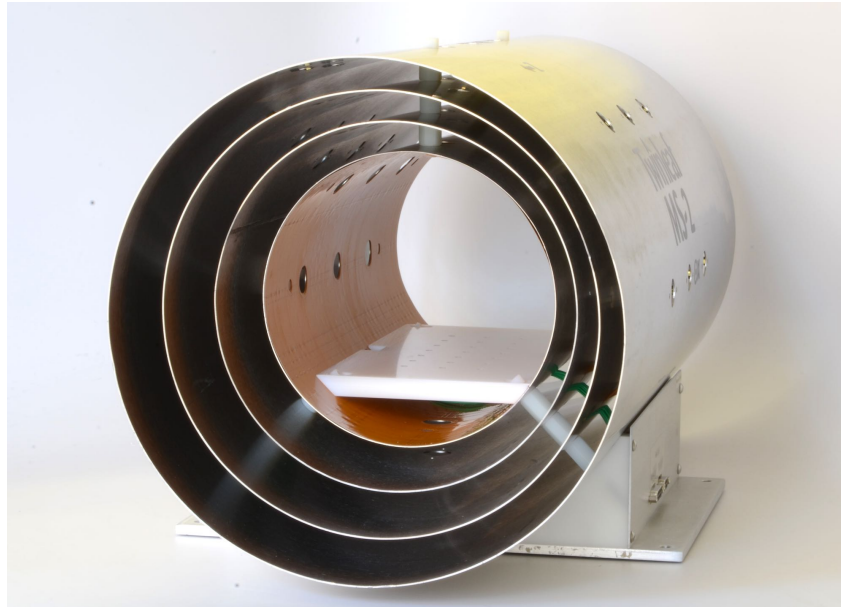
One possible way to characterize a magnetic shielding is to calculate its shielding factor.

### 2.2.1 Magnetic shielding factor

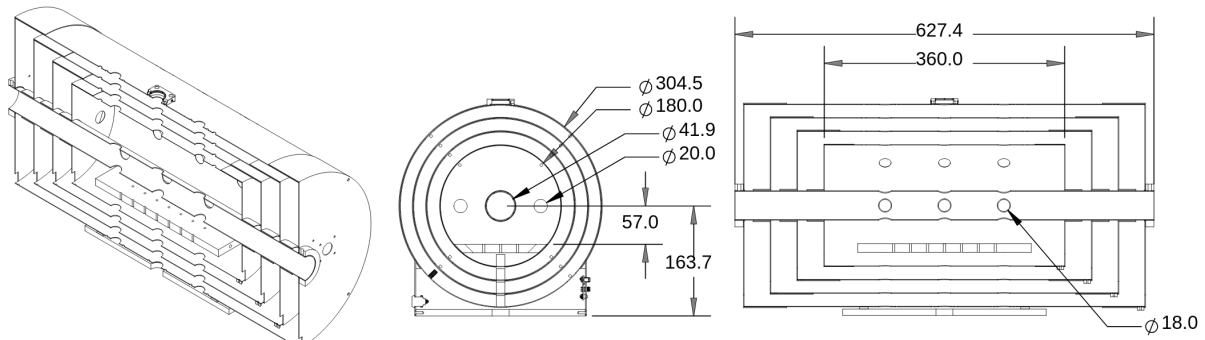
For measuring the magnetic shielding factor, the fields outside of a shielding have to be compared with the fields inside of the shielding:

$$S = B_{\text{ext}}/B_{\text{int}} \quad (2.3)$$

As source for the magnetic fields the room coils in ExWi B64 (Cryo lab) were used. These coils are mounted at the walls, the ceiling and underneath the floor of the laboratory and they build a large, square shaped 3D Helmholtz coil. From this large coil system, we used the component which generates magnetic fields across the laboratory and the normal of



(a) MS-2 shielding from Twinleaf [9]



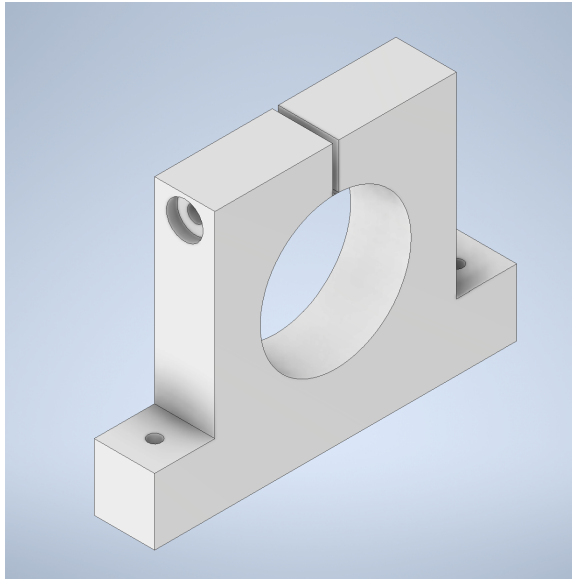
(b) Sketch with the dimensions of the shielding in mm [9]

Figure 2.8: Picture from the open magnetic shielding from Twinleaf with its four layers of mu metal and its dimensions

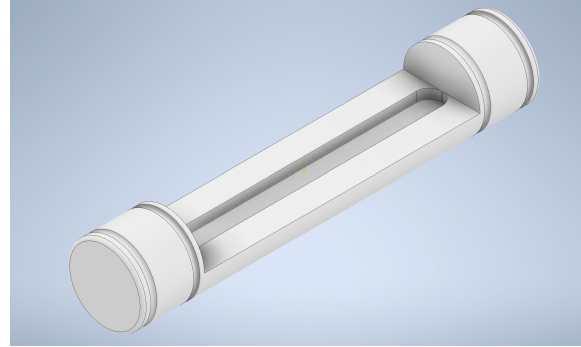
the coil's area has the same direction as the Z-axis of the mu metal and of the sensors inside the shield. Since the area of this coil is relatively big compared to the one from the round 3D Helmholtz coils 5.1, the magnetic fields were expected to act more homogeneous and therefore the position of the Rb sensors and the fluxgate would not change the signals as strongly as experienced with the alignment problems with the 3D Helmholtz coils.

For the creation of the magnetic fields again the WFG was used. The signal was a sinusoidal waveform which was lead to the KEPCO bipolar operational amplifier (model: BOP 20-20DL, S/N: E166092) and from there to the room coil.

Since the company states a shielding factor of about  $10^6$ , our fluxgates would not be able to measure the sinusoidal signals but the signal without shield is to high for the Rb



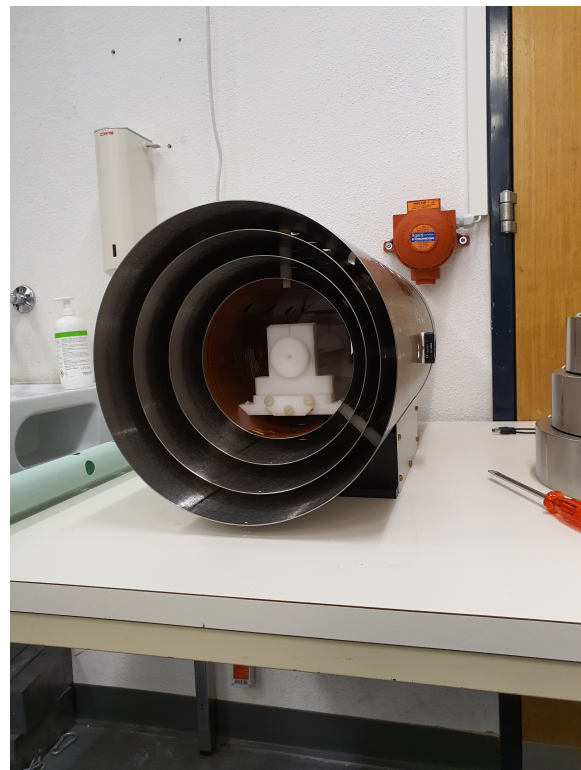
(a) Sketch of the holders feet



(b) Holder for the Rb OPM



(c) Fixation of the Rb sensors in the holder

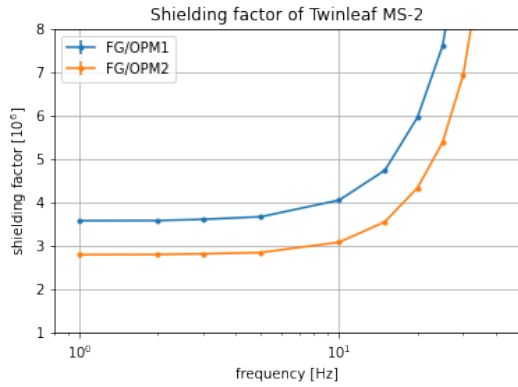


(d) Holder with the sensors inside of the MS-2

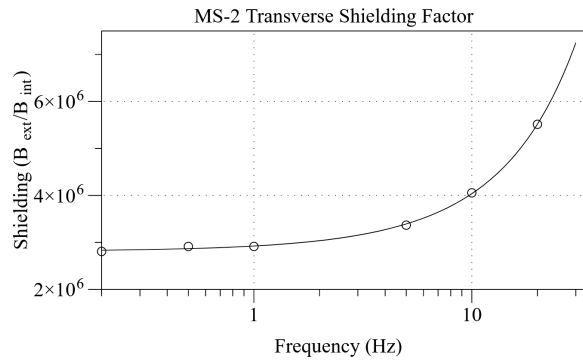
Figure 2.9: Holder for the Rb Sensors. From sketch to the finished version inside of the magnetic shielding.

sensors. Therefore, the Rb sensors were used inside of the mu metal shielding and the fluxgates were used outside. First the amplitude of the magnetic fields was measured

outside the shielding. Therefore, the shielding was removed from the table (since the presence of this shielding can also affect the magnetic fields outside of it), and at the same position and height as usually the Rb sensors are placed, a fluxgate was mounted. Then the signal from the fluxgate (Sensys FGM3D 1 mT, S/N 1990 [10]) was measured and the signals amplitude was extracted from this data. This measurement has been done at different frequencies, since the shielding is frequency dependent.



(a) Measured shielding factor



(b) Shielding factor from performance sheet [9]

Figure 2.10: Magnetic shielding factor of the Twinleaf MS-2. On the left is the measurement taken in our lab and on the right the stated shielding factor by the company

Afterwards the shielding with the Rb sensors inside was placed at its original location (where the fluxgate was placed), the same measurement as done with the fluxgate was repeated. Now we have the amplitudes of the magnetic field at the same position once inside of the magnetic shielding and once outside. For the shielding factor, only the fraction of both amplitudes was calculated for all frequencies.

Figure 2.10 is showing our result compared to the shielding factor stated from the company. We can confirm the stated shielding factor of  $10^6$ . Having a closer look at Fig. 2.10a, the second Rb sensor is matching the data from the company better for the lower frequencies and for the higher frequencies it is the first Rb sensor which is closer to the stated magnetic shielding factor by Twinleaf. Although this is still within the order of magnitude, this could be caused by the position of the Rb sensors inside the shielding and the position on the table. Even with the laser alignment device it was still not possible to place both, the fluxgate and the Rb sensors at the exact same position one after another. The error of this positioning lies within a few mm. This could have been tested by changing the position of both Rb sensors inside of the magnetic shielding.

Another possible explanation is that during the zeroing of the sensors they experienced small differences, causing the compensating fields to differ from sensor to sensor.

### 2.2.2 Internal coil characterization

The Twinleaf MS-2 has integrated coils, to e.g. compensate remanent magnetic fields or to generate signals inside of the shield as for the frequency response or amplitude scan measurements (see Sec. 2.1.4 or 2.1.5). The aim for this experiment was to check the calibration, stated by Twinleaf [9] and to know the amplitude of the applied signals.

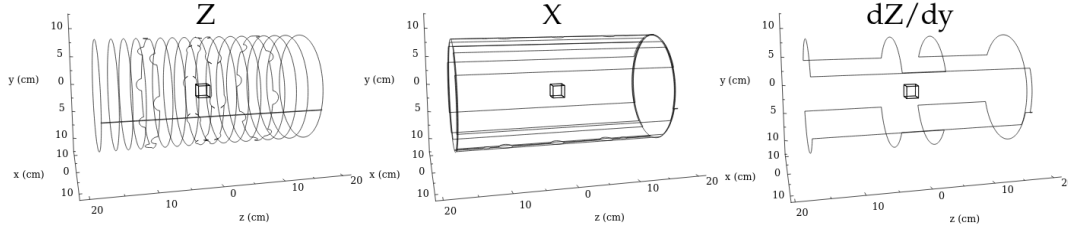


Figure 2.11: Structure of the coils inside of the magnetic shielding [9]. The axis of the internal coils correspond to the coordinate system (Fig. 2.1) of the Rb sensors. The coils construction for fields in Y axis is the same as for the X axis

Figure 2.11 is showing the configuration of the coils inside of the shielding for every axis. Twinleaf stated on their webpage, that these internal coils are calibrated as the follows:

- X/Y (vertical/transversal) coil calibration: 57.6nT/mA
- Z (longitudinal) coil calibration: 105 nT/mA

The Rb sensors were not able to measure such high magnetic fields because they would saturate at these amplitudes. Therefore fluxgates were used, which were sensitive in this range. The decision fell to the following two fluxgates:

- Stefan Mayer Industries FLC3-70 (S/N 2247) [11]
- Sensys FGM3D 125  $\mu$ T (S/N 2261) [10]

The fluxgates were placed inside of the shielding, its sensors as centered as possible. Once inside, both directions (Y and Z direction) were measured for each fluxgate in order to avoid any unnecessary movement of the fluxgate and a change of their position. The signals for the internal coil were generated from the WFG and then directed via a resistor to the internal coils interface.

For the first round only a few data points were taken. A 1 k $\Omega$  resistor was placed in the circuit. The settings of the WFG were:

- Frequency: 1 Hz and 40 Hz
- Amplitude: Scanned from 5 to 20 V
- Offset: no offset



- Phase shift: no phase shift

The goal of this measurement was, to compare the behavior of both fluxgates and to decide with which one to continue for a finer amplitude scan.

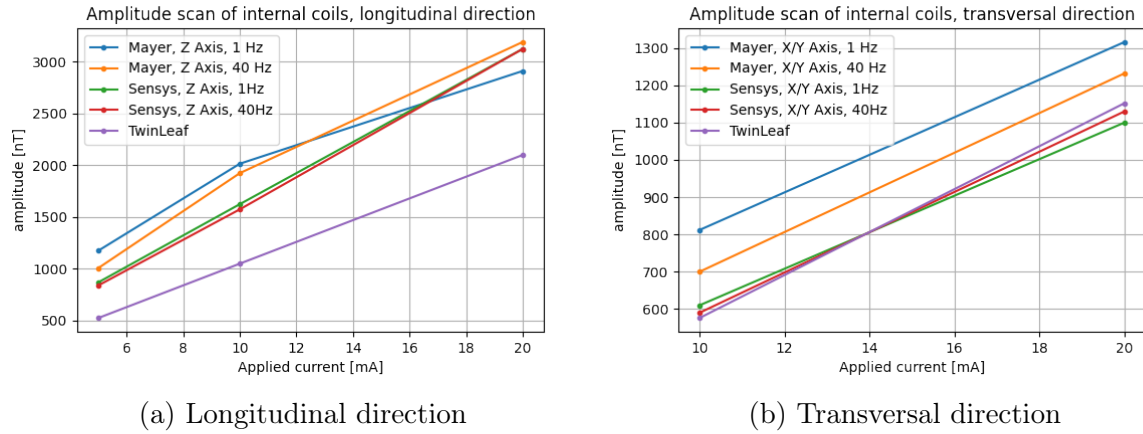
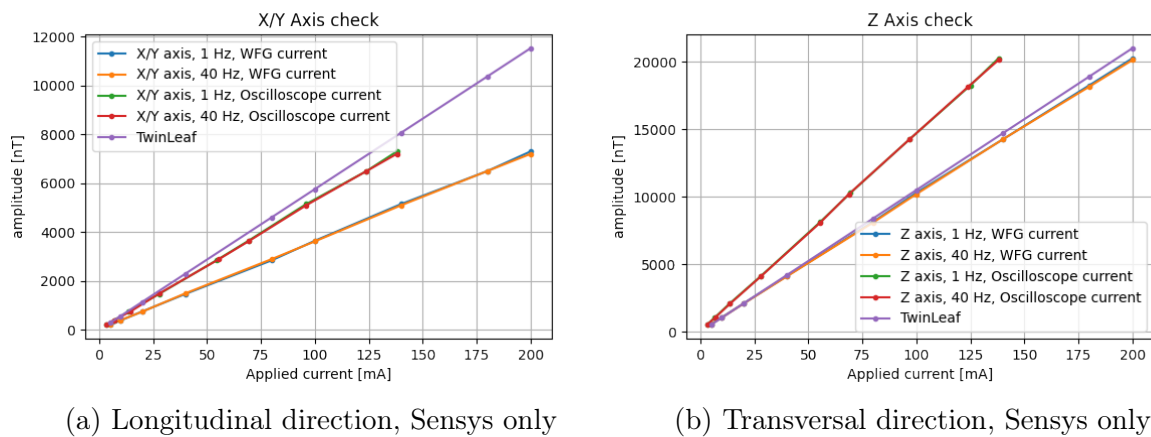


Figure 2.12: Amplitude scan with the internal coils. The scan was performed with two different frequencies and with two different fluxgates.

In Fig. 2.12 the results of the first round are visible. Only the Sensys fluxgate in Y direction matched the predicted amplitude partly. Therefore, the fluxgate from Sensys was used for further experiments. Stefan Mayers fluxgate was in almost all cases further away from the stated magnetic fields from Twinleaf. Additionally the fluxgate showed a strange change of the slope, as seen in Fig. 2.12a.

An additional error source could be the WFG. In the second measurement the WFG's signal was also crosschecked with an oscilloscope. The experiments were continued with the fluxgate from Sensys. Also the number of data points was increased. The resistor was replaced with a 100  $\Omega$  resistor, to increase the range of the applied currents.



(a) Longitudinal direction, Sensys only

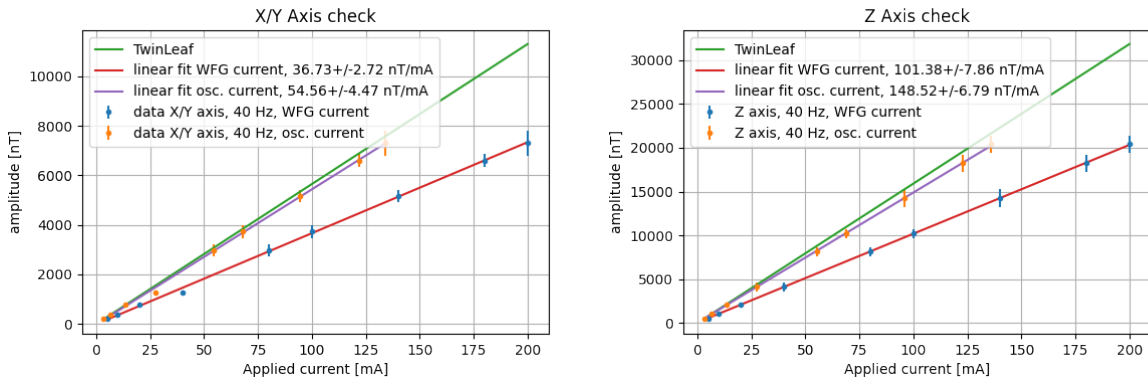
(b) Transversal direction, Sensys only

Figure 2.13: Fine amplitude scan of the internal coils with the Sensys fluxgate.

During the measurement there was something noteworthy. The difference of both amplitudes, once shown at the WFG and once at the oscilloscope, increased by the same factor as the amplitude itself was increased. Therefore, I decided not only to read the voltage from the WFG but also to note the voltages measured by the oscilloscope and to compare the data in the end.

All the results in Fig. 2.13 look more or less linear. The only difference is the slope between the readout applied currents from the WFG and the oscilloscope. The 1 Hz and 40 Hz signals are the same within the errors. In Fig. 2.13a the slopes from the oscilloscope read out signals match the stated slope from Twinleaf much better, whereas in Fig. 2.13b the slopes read from the WFG match better. A possible explanation to this phenomena is that the fluxgates were fixed inside of the shielding. When changing the direction of the applied magnetic fields, the fluxgates were left at the same position. The sensor positions inside the fluxgate are not located in the same spot. Therefore, this difference of the magnetic fields could be explained by the different positions of the sensors inside the fluxgate.

To investigate the strange behavior as seen in Fig. 2.13a, the measurement has been repeated. This time it was possible to move the fluxgate in between the direction changes. But after finishing the data processing, the same result came out. The problem was not the execution of the experiment. The error source was found when changing the direction of the applied magnetic currents at the interface of the MS-2. After correction, the final result was more feasible than the first one.



(a) Longitudinal direction, Sensys only

(b) Transversal direction, Sensys only

Figure 2.14: Fine amplitude scan of the internal coils with the Sensys fluxgate

The problem was not the measurement itself, but the calibration factor. Twinleaf stated on their Website [9] a different calibration than it was written on the MS-2 in our lab. With the following calibration, the test in Fig. 2.14 succeeded and the calibration was verified with the following correct calibration:

- X/Y (vertical/transversal) coil calibration: 56.5 nT/mA
- X/Y (vertical/transversal) measurement:  $(54.6 \pm 4.8)$  nT/mA

- Z (longitudinal) coil calibration: 159.2 nT/mA
- Z (longitudinal) measurement: (148.5  $\pm$  6.8) nT/mA

The measured calibration for the X/Y direction matches the expected value of 56.5 nT/mA within the error. Unfortunately, the measured value for the coil calibration in Z direction does not match the expected 159.2 nT/mA as good as in the X/Y direction. The error source could be that the current read on the oscilloscope is not completely correct but this was not checked.

## 2.3 Radiofrequency (RF) shielding

Most of the noise in the measurements is coming from electronic devices in the laboratory with a peak at 50 Hz and since our building is right next to the train station we also experience magnetic noise coming from the high voltage line of the Swiss federal railways with its peak at 16.8 Hz. These peaks are clearly visible when performing a Fast Fourier transform of an arbitrary background scan (see Sec. 2.1.3).

The RF shield is meant to decrease the amplitudes of the noise at those frequencies as a passive shield. Therefore we wanted to construct this RF shield surrounding of the mu metal shield as an additional layer.



Figure 2.15: Process from sketch to the finished RF shield: The left picture is showing the sketch of the RF shield before ordering the materials. The center picture is showing the assembly of the shield with Item profiles and aluminium plates. The picture on the right shows the finished RF shield containing the Twinleaf mu metal shielding and the Rb-OPMs.

For the RF shield aluminium plates with a thickness of 6 mm were used. For the stabilization of these plates we used Item profiles made of aluminum. Four Item profiles with the dimensions of 40 mm x 40 mm x 820 mm and eight of the dimension 40 mm x 40 mm x 420 mm were used for the framework. Four Plates of aluminum with areas of 820 mm x 420 mm and two with areas of 420 mm x 420 mm were placed between the profiles, as it can be seen in Fig. 2.15.

After a few test measurements it was clear that this layer of 6 mm aluminum was insufficient as a standalone RF shielding. Therefore an additional layer of 5 mm thick iron was added, surrounding the aluminium layer with a separation of 18 mm (see Fig. 2.16).



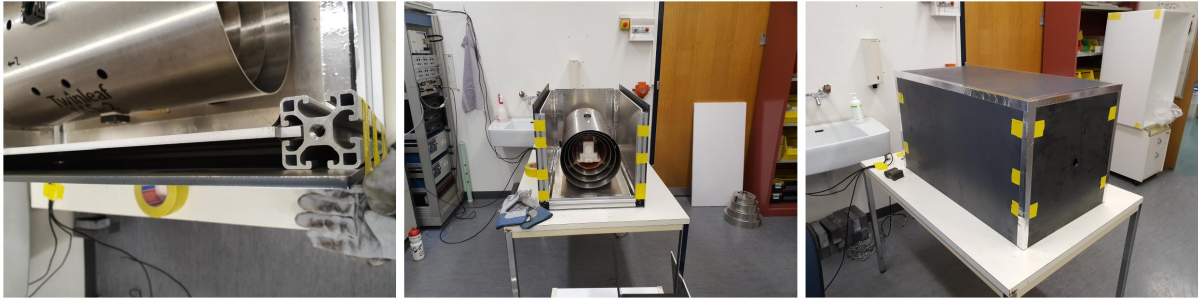


Figure 2.16: The picture on the left is showing the inner aluminium layer surrounded by the iron layer. The picture in the center shows, how the mu metal shielding is placed inside of the RF shielding. The picture on the right is showing the final RF shielding from the outside.

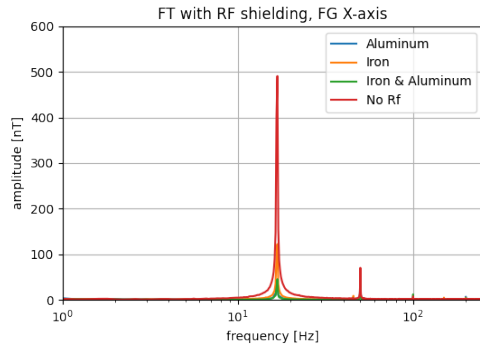
For the characterization of the RF shielding it was necessary to measure only inside the RF shield and not inside the mu metal shield. Again the fluxgate from Sensys were used for this task. For the characterization, two measurements were performed. The first measurement was a background measurement with different configurations of the RF shield. The fluxgate were placed inside the RF shield in that way, that the axis written on the fluxgate match the coordinate system from the removed mu metal shield. As in Sec. 2.1.3, the measurement was repeated 100 times for better results in the Fourier transform.

The plots in Fig. 2.17 are showing the whole spectra in the left column and a zoomed rectangle at 50 Hz for each direction next to it. The right column with the zoomed section is showing nicely how aluminum and iron are suppressing the fields at lower frequencies. For all three directions the combination of iron and aluminium is suppressing the signal as expected. But this expected behaviour was only shown for the 50 Hz peak in Fig. 2.17. Figure 2.18 is showing the 16 Hz peak next to the full spectra of the background measurements and the results completely disagree with the expected behaviour.

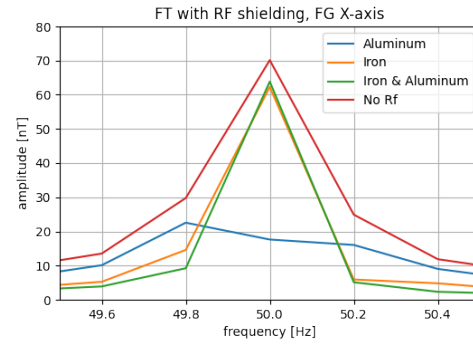
The second method was to perform frequency scans for all three directions with all RF shielding options. The aim was to calculate the suppression factor depending on the signal's frequency. Other than the first method with the background scan, now artificial fields were required. They were produced with the WFG, lead to the KEPCO amplifier powering the room coils. The geometry of the room coils was described in Sec. 2.2.

Since it was not possible to either turn the room coils nor to move the shielding without having to disassemble the RF shielding every time, the field direction was only induced in Z (longitudinal) direction. The data of the sensors in the other direction was gathered anyway and the results of the frequency scans are presented in the left column of Fig. 2.19. With all four configurations one can now calculate the suppression factor of each set up. Dividing the signals without any RF shielding by the signal of each configuration will result in the suppression factor as shown in the right column in Fig. 2.19.

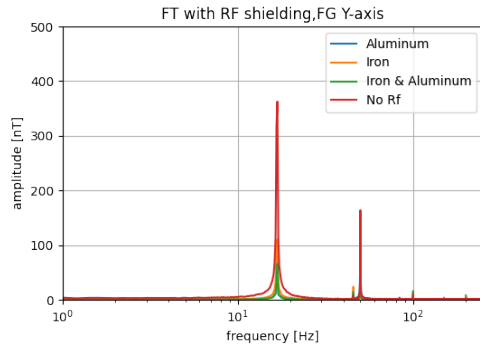
In both, Fig. 2.17 and Fig. 2.19, it is visible that in almost every case the combination of iron and aluminum has the best suppression of radio frequencies.



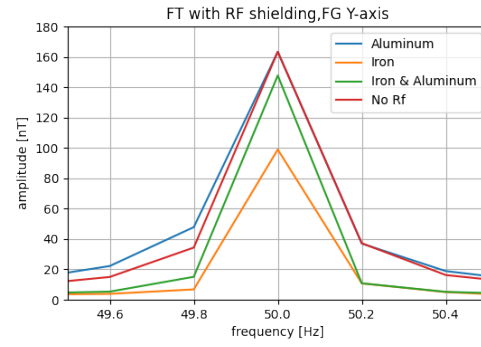
(a) Vertical direction



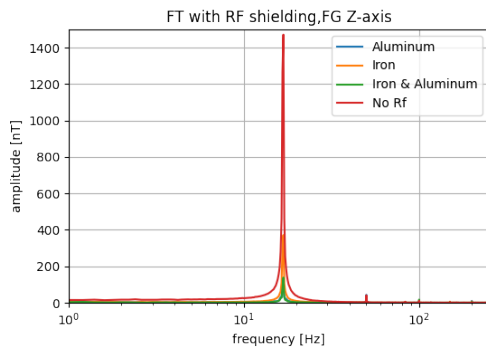
(b) Zoomed view on 50 Hz peak



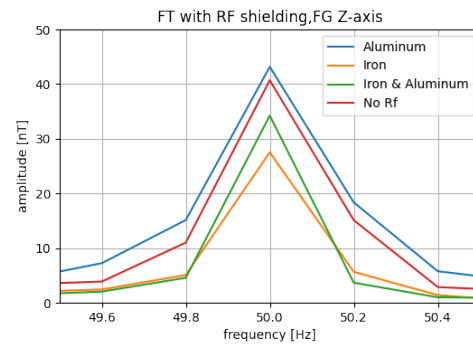
(c) Transversal direction



(d) Zoomed view on 50 Hz peak

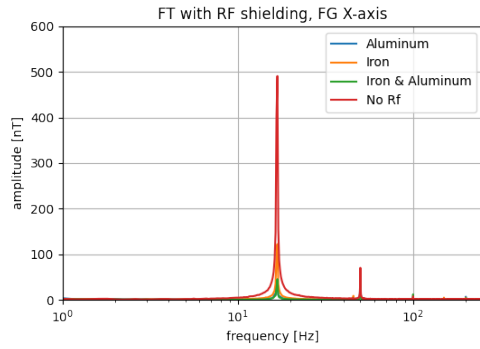


(e) Longitudinal direction

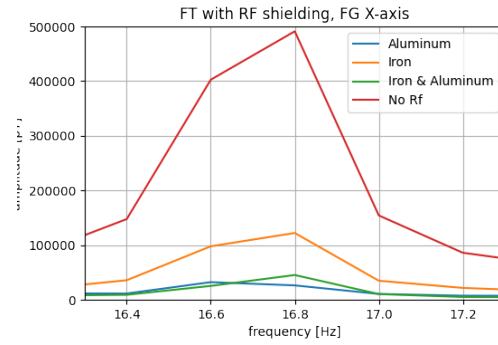


(f) Zoomed view on 50 Hz peak

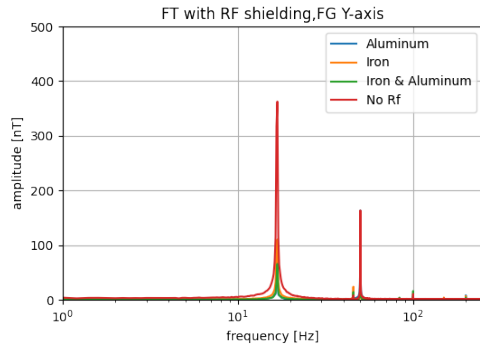
Figure 2.17: Mean of all runs. The left column is showing the whole spectra of signals, whereas the right one is showing only the peak at 50 Hz corresponding to the direction of the left column.



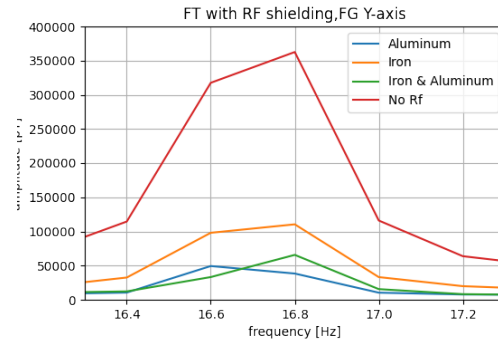
(a) Vertical direction



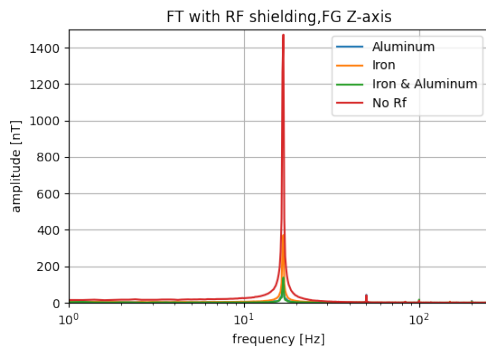
(b) Zoomed view on 16 Hz peak



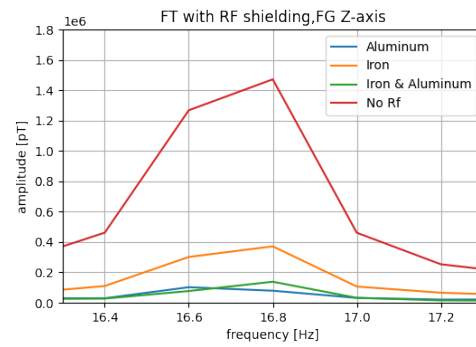
(c) Transversal direction



(d) Zoomed view on 16 Hz peak

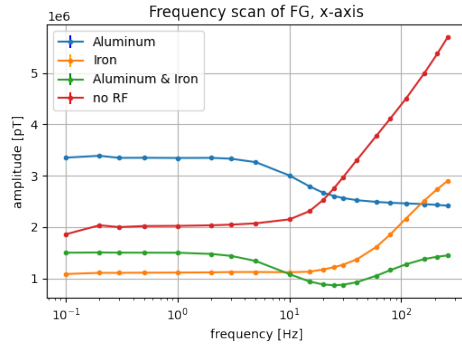


(e) Longitudinal direction

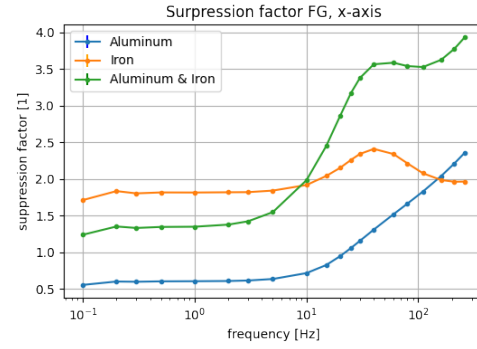


(f) Zoomed view on 16 Hz peak

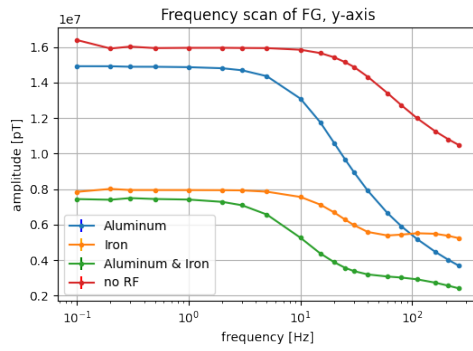
Figure 2.18: Mean of all runs. The left column is showing the whole spectra of signals, whereas the right one is showing only the peak at 16.8 Hz corresponding to the direction of the left column.



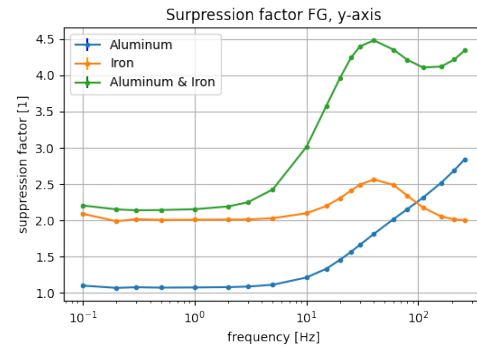
(a) Freq. scan vertical axis



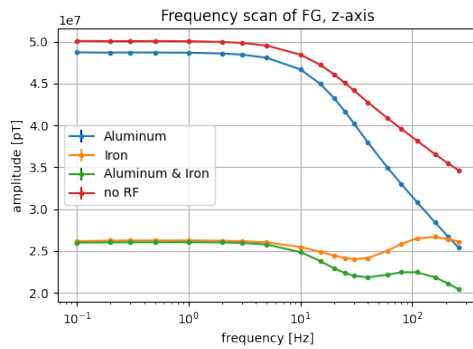
(b) Suppression vertical axis



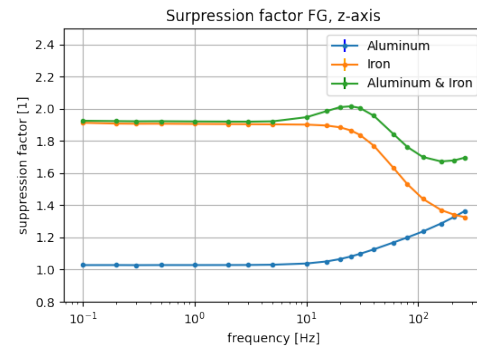
(c) Freq. scan transversal axis



(d) Suppression transversal axis



(e) Freq. scan longitudinal axis



(f) Suppression longitudinal axis

Figure 2.19: Frequency scans and suppression factors of all axes with all constellations

## 2.4 Additional measurements

### 2.4.1 Stability measurements

How do the sensors and the magnetic shielding behave when measuring for a longer period of time? To give an answer to this question, a longer stability measurement has been performed. The Rb sensors inside of the mu metal and RF shielding with the iron and aluminium configuration were running for at least three days. As to not have any trouble with the amount of data, the sample rate was set to 10 Hz.

The result from the first stability test did not look very well. Figure 2.20 shows a strong, periodical drift of over 100 pT per day.

To probe if the temperature is responsible for the fluctuation, an additional thermic shielding made out of styrofoam and two temperature logger, one inside of the thermal shield and one outside, were installed. The styrofoam was wrapped around the mu metal shielding and was inside the RF shield, since I expected the mu metal to be the source of these high drifts in the magnetic fields. The measurement was repeated for almost the same time interval.

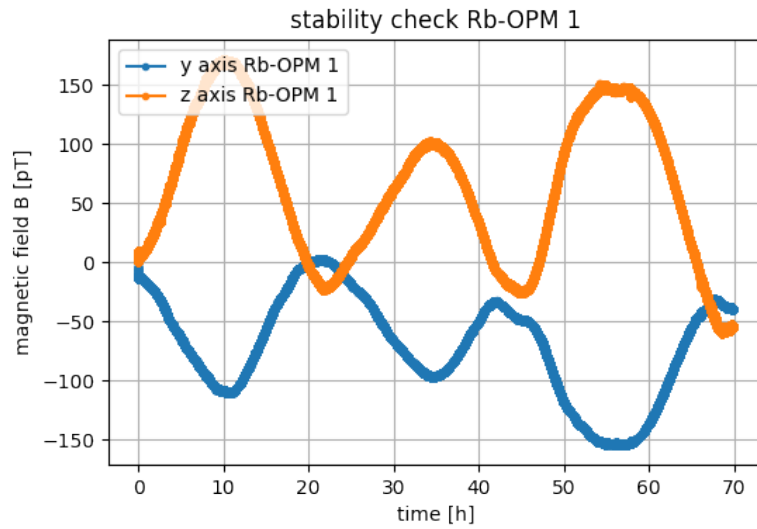
After the results in Fig. 2.21 it was clear, that the temperature drifts in the lab are causing the fluctuations of the magnetic field. But does it come from the mu metal, aluminium or iron layers? Therefore we repeated the same experiment, this time only with the mu metal shielding and disassembling the RF shielding.

It became also clear that the layer of styrofoam is not performing really well to keep the temperatures stable. The Allan standard deviation for the temperature stability in Fig. 2.21 is showing that with the smaller deviations for the internal temperature sensor, especially at smaller time intervals  $\tau$ . Also in the upper plot in Fig. 2.21 it is nicely visible, that it only delays the temperature rises and falls, but it does not damp them enough.

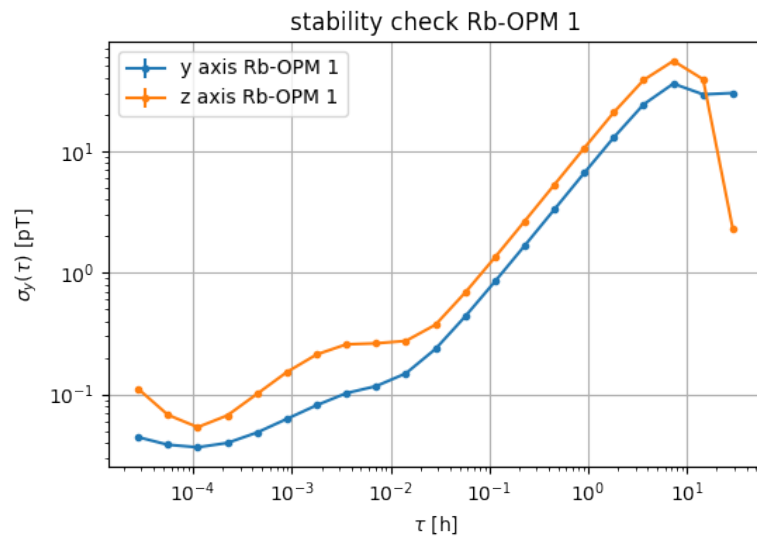
Removing the RF shielding resulted in the same behavior as before. Figure 2.23 is showing the comparison of the Allan standard deviation of both measurements. It is clearly the mu metal shielding which causes the high magnetic field drifts, since there is no big difference in both plots in Fig. 2.23. After the calibration process of the sensors one could easily force a drift of several pT by only laying the hand on the shielding and giving some extra heat to it.

In both measurements, the one with and the one without RF shielding, show in their Allan standard deviations how the fluctuation of the magnetic fields follows the fluctuation of the temperature. Figure 2.21 shows this behavior very good. The temperature has its maximum deviation at a time interval of about 10 h, whereas the maximum deviation of the magnetic fields is at the lower time interval of 7.5 h.

The consequence of this measurement: If longer measurements were planned with the Rb OPMs, a proper thermal shielding or something else to stabilize the temperature of the mu metal shielding is needed. Another possible solution would be to characterize these drifts as a function of temperature and to measure additionally to the experiment the temperature of the shielding's surrounding and then to correct the raw data.

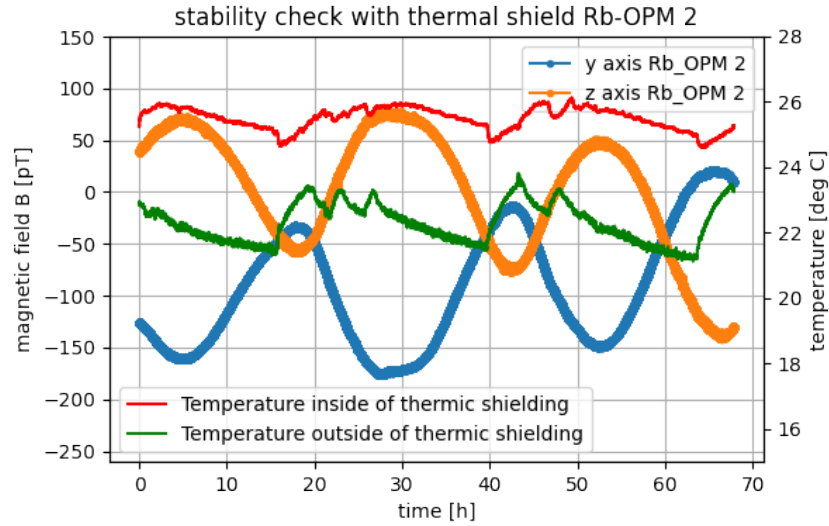


(a) Signal from one of the Rb sensors over a range of few days

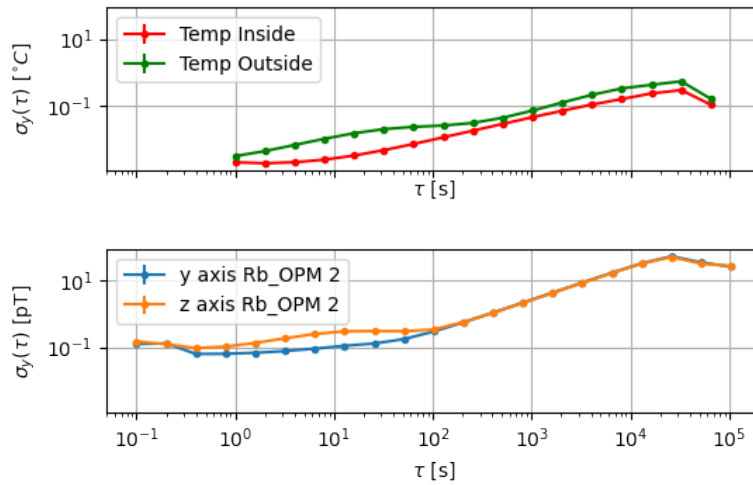


(b) Allan standard deviation from the measurement

Figure 2.20: First test measurement to see the behavior of the sensors letting them run over a few days.

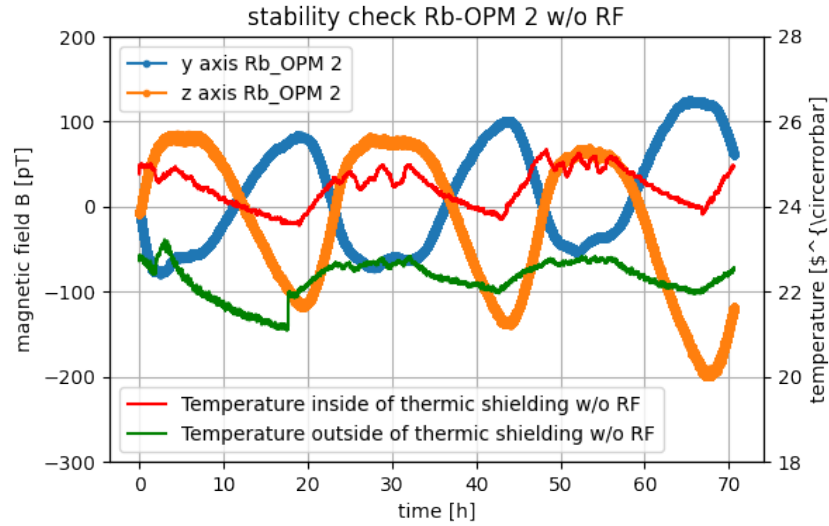


(a) Signal from one of the Rb sensors with the thermic shielding and with RF shield

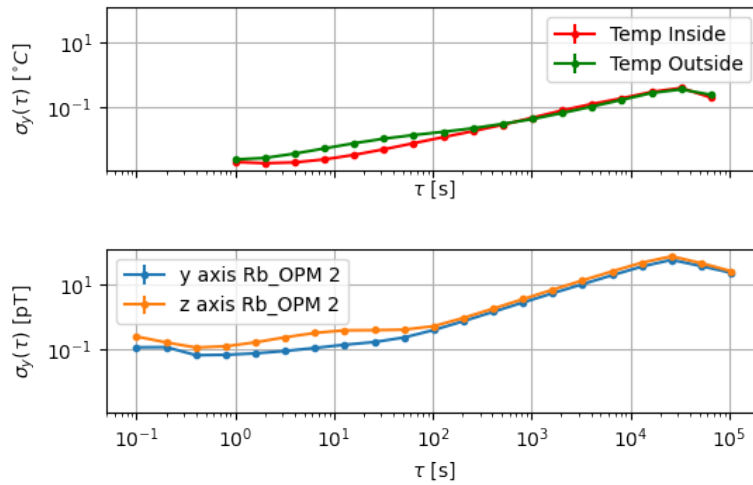


(b) Allan standard deviation from the measurement with the thermic shielding and RF shield

Figure 2.21: Measurement with the thermic shield and with the RF shield: Signal from one of the Rb sensors over a range of a few days with temperature values



(a) Signal from one of the Rb sensors with the thermic shielding but without the RF shield



(b) Allan standard deviation from the measurement with the thermic shielding but without RF shielding

Figure 2.22: Measurement with the thermic shield and without the RF shield: Signal from one of the Rb sensors over a range of a few days with temperature values



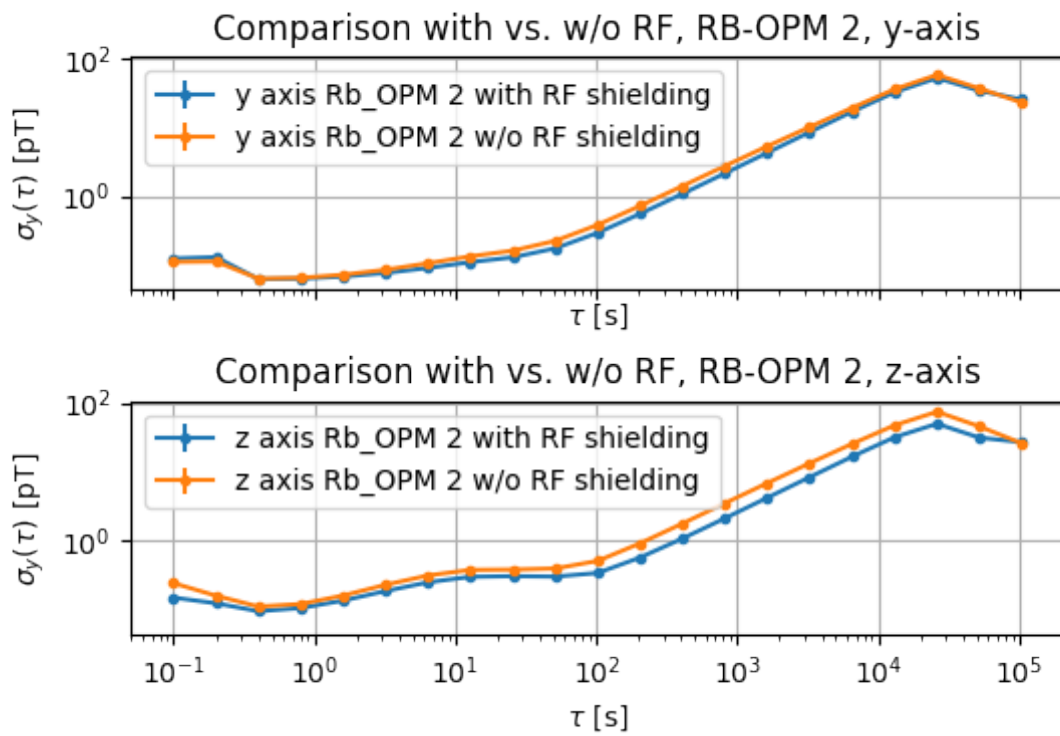


Figure 2.23: Comparison of the Allan standard deviation from the stability measurements without and with the RF shielding

### 2.4.2 Simulating the heart beat

Let us jump back to the introduction in Sec. 1.1, the magnetic fields of the human body. The aim in this experiment was to check the feasibility of detecting magnetic signals from the human heart.

Depending on the size of a subjects heart, a fieldstrength between 10 and 100 pT are normal. In the WFG there was an arbitrary waveform function programmed, called "CARDIAC.arb" [12] which mimics the heart' signal. Through a  $1\text{ M}\Omega$  resistor the signal was lead to the internal coil interface of Twinleaf's MS-2. Inside of our magnetic shielding, which also was equipped with the RF shielding, both Rb sensors were placed near each other. The chosen channel was the one in Y (transversal) direction, since here we had the best shielding factor of  $4 \cdot 10^6$  (Sec. 2.2.1) and also as seen in Sec. 2.1.3, the background noise of the 16.8 Hz was strongly suppressed.

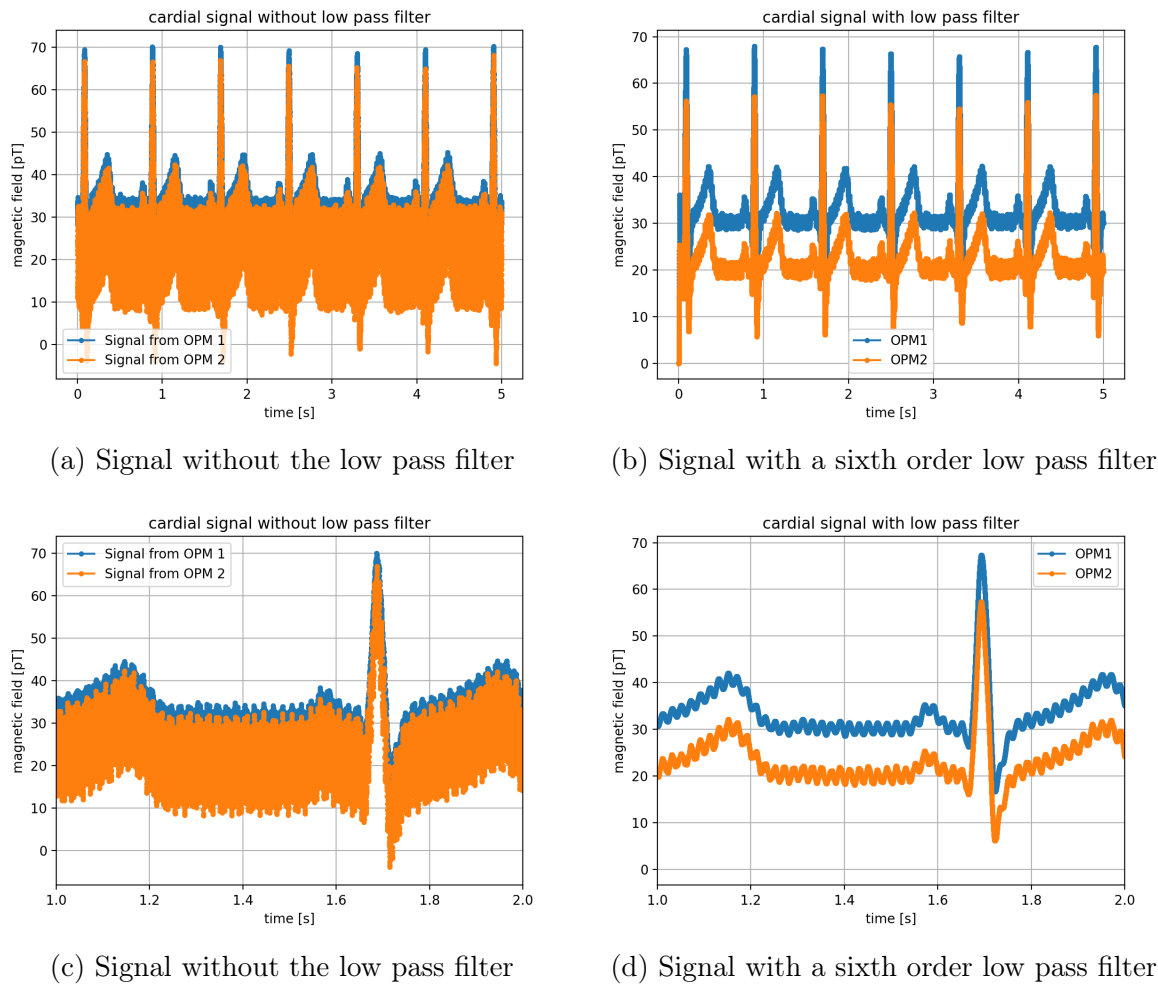


Figure 2.24: Measuring cardiac signals

With a sample rate of 10000 Hz the Rb sensors measured for five seconds respectively. On the left hand side in Fig. 2.24, the raw data of one run is presented. In the lower

row, a one second wide rectangle of the whole plot is shown. The SNR is very bad. After processing the data through a sixth order Butterworth low pass filter, as it is used in the digital output of electronics (see Sec. 2.1.1), the noise is almost completely suppressed, leaving only the 50 Hz noise of the electronics.

Focusing on the right hand side of the plots in Fig. 2.24, the maximum peak-to-peak part of the signal reaches 50 pT, which is clearly visible, even without an applied low pass filter. The remaining smaller curves of the signal in regimes of 5-10T are also nicely visible, but only with the applied low pass filter.

# Chapter 3

## Results and discussion

The main goal of the characterization was to check the applicability of one or several Rb OPMs in medical applications as support and extension of the well known electric currents, which are produced in the human bodies.

A proper shielding is indispensable. Although the QuSpin's Rb OPMs have their internal coils for compensation of the remanent magnetic fields, this only works flawlessly having fields below nT range.

Also the choice of material is crucial. For most magnetic fields, a multilayer Mu metal shielding is enough. With an additional RF shielding, as in our case the combination of iron and aluminium, also the lower frequency noise is damped. As seen in section 2.4.1, also the temperature of the shielding has a high effect on the remanent magnetic fields inside of the shielding. Another important thing is the stabilization of the temperature of the shielding material to avoid big drifts, especially for longer measurements.

The remaining magnetic fields, after the installation of the magnetic shield can then still be characterized as it had been done with the background scan in section 2.1.3. The decision whether reading out the digital or analog data is also important. As mentioned in section 2.1.1, the USB digital output has only a sample rate of 200 Hz, but has on the other hand an inbuilt sixth order low pass filter implemented. Reading out the analog data, one can increase and adapt the sample rate, but one has to keep in mind that with a higher sample rate, the signal gets noisier. A self implemented low pass filter helps, to keep the signal to noise ratio to the same level as from the digital output.

The digital output is limited to a sample rate of 200 Hz. Therefore the optimal bandwidth is 100 Hz. This is also the expected regime of biological magnetic fields of the human body. Since we wanted our own piloting and DAQ software, which can be run remotely and with a higher sample rate, the attenuation of the signal had to be checked with rising frequencies. Section 2.1.4 has shown, that the -3 dB mark is even above the 200 Hz signals, so these aspects should not pose difficulties.

With all these requirements being fulfilled, there should be no major problems facing a project to measure human magnetic fields with this new optical pumped magnetometers with a Rubidium vapor cell. For future experiments on living subjects, a mu metal shielded room is necessary as the Twinleaf shield is too small for a human.

# Chapter 4

## Introduction

### 4.1 Motivation: Axions and producing fake axion fields

In the Standard Model (SM) of particle physics, symmetries are fundamental. The three discrete symmetries, charge conjugation  $C$ , parity  $P$  and time reversal  $T$  were thought to be fundamental properties of the universe until 1956, where Wu et al. showed the parity violation in the beta decay of  $^{60}\text{Co}$  [13]. In 1964 Christenson et al. reported that also  $CP$  symmetry is violated by the Kaon decay [14]. The combination of all three symmetries, the  $CPT$  symmetry, is thought to be conserved to the present day. The  $CPT$  theorem [15] predicts from theoretical foundations that "under mild assumptions [...]  $CPT$  is an exact symmetry of local Lorentz-invariant field theories of point particles." [16]

The violations of symmetries [17] had a great influence on the SM and are even today interesting tests. I.e. from cosmology still unknown sources of symmetry violation could be discovered, at least there are some indications. A big question from this field is why there is no observable antimatter in the universe. Andrei Sacharov proposed the three famous conditions that baryon-generating interactions, to produce the observable universe, have to satisfy to produce baryons and antibaryons at different rates and the resulting asymmetry between matter and antimatter: baryon number violation,  $C$  and  $CP$  symmetry violation and a departure from thermodynamic equilibrium [18, 19]. In the SM the  $CP$  violation is known, for example in the  $K$  and  $B$  meson decay [20]. These violations are included to the SM with a phase in the Cabibbo-Kobayashi-Maskawa (CKM) matrix [21]. The CKM matrix relates the weak interaction eigenstates of quarks with their mass eigenstates. There are 4 free parameters for the three quark families. Three of them are the quark mixing angles and the fourth is a phase factor which is responsible for the contribution to the  $CP$  violation in the electroweak SM.

The processes in the weak sector of the SM which are responsible for  $CP$  violation are insufficient to explain the existing asymmetry between matter and antimatter in the universe. Apart from the  $CP$  violation in the weak sector of the SM, there exists also a  $CP$ -odd term in the Lagrangian defining the vacuum state in quantum chromodynamics (QCD). This  $CP$ -odd term is a mixing angle  $\theta_{QCD}$  which has to be yet determined and its value should lie between 0 and  $2\pi$  [20]. The prediction of the electric dipole moment

for the neutron resulting from  $CP$  violation[20]:

$$d_{n,\text{QCD}} = \theta_{\text{QCD}} \cdot 10^{-16} e \cdot \text{cm}. \quad (4.1)$$

The neutron EDM is experimentally determined [22] to be

$$|d_n| \leq 1.8 \cdot 10^{-26} e \cdot \text{cm} \quad (4.2)$$

It follows that  $\theta_{\text{QCD}}$  must be very small, or fine tuned close to 0 to match the current upper limit for the neutron EDM. Despite the rather high expected value for the neutron EDM from the theory, no neutron EDM has been found to the present day. This is known as the strong  $CP$  problem and many solutions have been proposed, which also include additional  $CP$  violation terms. One of these solutions is the Peccei-Quinn theory, which proposes the existence of the axion [23]. It introduces a new field, with the same name axion [17].

## 4.2 Resonance Measurements

This section will introduce resonance measurements as the Rabi technique (Sec. 4.2.1) and the Ramsey technique (Sec. 4.2.2) considering neutrons. In Sec. 4.3 it is explained, what influence an additional time dependent magnetic field has on neutrons in a Ramsey measurement and why we use it to mimic axion fields.

### 4.2.1 Rabi technique

With the Rabi Method the magnetic moment of nuclei can be measured [24, 25]. It is named after the setup used by Isidor Isaac Rabi which consists of a static magnetic field  $B_0$  along the beamline and a single resonance spin flipper, as it can be seen in Fig. 4.1. To separate the two spin states, two inhomogeneous fields are placed before and after the spin flipper (Stern-Gerlach apparatus) which serve as polarizer and analyzer.

$$P_{\text{flip}} = \frac{\omega_1^2}{\Delta\omega^2 + \omega_1^2} \sin^2 \left( \frac{\tau}{2} \sqrt{\Delta\omega^2 + \omega_1^2} \right); \quad \omega_1 = -\gamma_n B_1 \quad (4.3)$$

Starting from the spin flip probability (which is derived from applying a time evolution operator on a time independent Hamiltonian for a magnetic moment interaction of a spin 1/2 particle) in Eq. (4.3) where  $\tau$  states the interaction time of the neutron inside of the spin flipper, we notice how it simplifies if we use the spin flipper at the Larmor frequency ( $\Delta\omega = 0$ ), which leads to

$$P_{\text{flip}} = \sin^2 \left( \frac{\tau}{2} \omega_1 \right) \quad (4.4)$$

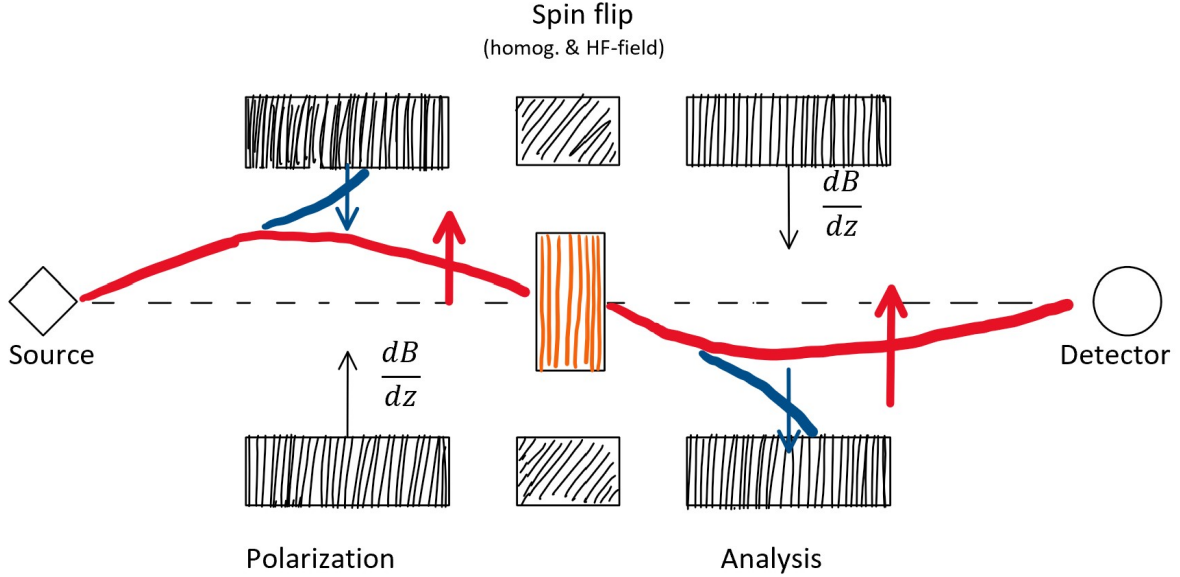


Figure 4.1: Schematic of a Rabi based setup: Two inhomogeneous magnetic fields serve as polarizer and analyzer. In between them, a resonance spin flipper surrounded by a homogeneous static magnetic field  $B_0$ , performs a  $\pi$  flip.

To maximize the probability for a spin flip, two conditions must be met.

$$\Delta\omega = 0 \quad (4.5)$$

$$\tau\omega_1 = \pi \quad (4.6)$$

To be precise  $\tau\omega_1 = (2n - 1)\pi$  would maximize for any integer  $n \geq 1$ , but not without increasing  $\omega_1$  accordingly. It also implies a flipping angle of  $(2n - 1)\pi$ . The second condition actually demands that for different interaction times  $\tau$ , the rotational magnetic field amplitude in the spin flipper  $B_1 = -\omega_1/\gamma_n$  is adjusted according to

$$B_1 = -\frac{\pi}{\gamma_n\tau}. \quad (4.7)$$

The interaction time  $\tau$  is constant for a monochromatic beam and the spin flipper can operate with a sinusoidal signal, with the frequency set by the Larmor frequency according to the static magnetic field  $\omega_0 = -\gamma_n B_0$ .

### 4.2.2 Ramsey Technique

By adding an additional spin flipper in the beamline and a certain distance in between the two spin flippers one obtains the setup for Ramsey interferometry [26] as shown in Fig.4.2. The benefits of Ramsey's method over Rabi's are, that for the same operating frequencies, Ramsey's method achieves a much higher sensitivity due to the fringe pattern. It is also

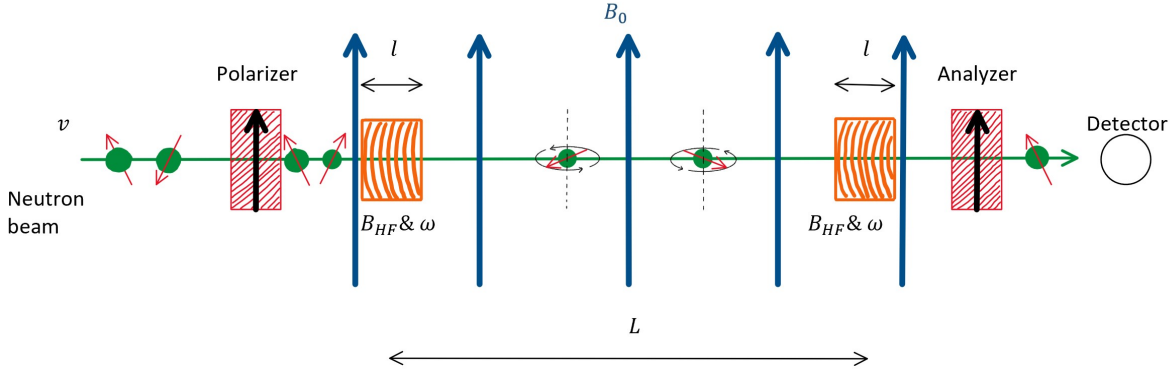


Figure 4.2: Schematic of a Ramsey setup: The similarities to the Rabi setup in figure 4.1 are the polarizer and analyzer. But there is an additional spin flipper and a interaction length  $L$  with a constant magnetic field  $B_0$  which allows the free precession for the neutrons.

independent of the velocity which is not the case for the Rabi technique.

Instead of a single resonance spin flipper contributing a  $\pi$ -pulse, the two spin flippers perform separately a phase-locked  $\pi/2$  pulse. In the intermediate space between the spin flippers neutrons precess about the constant magnetic field  $B_0$ . Both spin flippers should be operated at the same frequency with a set phase difference  $\delta\phi$ . If the frequency is set to the Larmor frequency (at resonance) and the phase is  $\delta\phi = 0$ , the spin flippers and the neutron precession stay synchronous during the flight time  $T$  between the spin flippers. The second spin flipper picks up the neutron at the same position, where it left the first spin flipper and completes the  $\pi$ -flip.

An existing phase difference ( $\delta\phi \neq 0$ ) between the neutron precession and second spin flipper would result in not completing the  $\pi$ -flip or even rotate back by  $\pi/2$ . There are many reasons for the neutron to pick up additional phase. The most obvious case is when  $\Delta\omega \neq 0$ , so the spin flippers are not operated at the resonance frequency. Other effects would be the contribution of the  $\vec{v} \times \vec{E}$  effect to the precession frequency, an inhomogeneous static magnetic field  $B_0$  between the two spin flippers or the contribution of the electric dipole moment in an electric field. Also other, more exotic interactions like the axion-gluon coupling could lead to a phase difference.

If the phase  $\delta\phi$  would be scanned from 0 to  $2\pi$ , the flipping probability would firstly start to decrease until it reaches a minimum at  $\delta\phi = \pi$  and then rise again to a maximum at  $\delta\phi = 2\pi$ . This pattern is repeating and giving rise to fringes that indicate a phase difference of  $2\pi$ . Since the collected phase during the free precession is  $\phi = \omega_0 T$ , assuming a constant  $\omega_0$ , the width of the fringes is inversely proportional to the free precession time  $T$ . For large  $\Delta\omega$ , the envelope of the fringes is decreasing as well and is following the shape of the Rabi spin flipping probability. The spin flipping probability in a Ramsey measurement is given by:



$$P_{\text{flip}} = \frac{4\omega_1^2}{\Omega^2} \sin^2\left(\frac{\Omega\tau}{2}\right) \left[ \frac{\Delta\omega}{\Omega} \sin\left(\frac{\Omega\tau}{2}\right) \sin\left(\frac{T\Delta\omega}{2}\right) - \cos\left(\frac{\Omega\tau}{2}\right) \cos\left(\frac{T\Delta\omega}{2}\right) \right]^2 \quad (4.8)$$

Since the width of the fringes is inversely proportional to the free precession time  $T$ , the frequency resolution may be increased further by extending the free precession time. Compared to Rabi's method, this can be done relatively simply. For Rabi's method, the peak width is inversely proportional to the interaction time  $\tau$ .

### 4.3 Ramsey scan with a time dependent $B_a$ field

Additionally to the classic Ramsey setup, which was built up at the NARZISS beamline, with its static magnetic field along the interaction zone, which is responsible for the precession of the neutrons in between the two spin flippers, an oscillating magnetic field source was attached (see Fig. 4.3). With this time dependent magnetic field  $B_a(t)$ , the precession of the neutrons is not constant anymore.

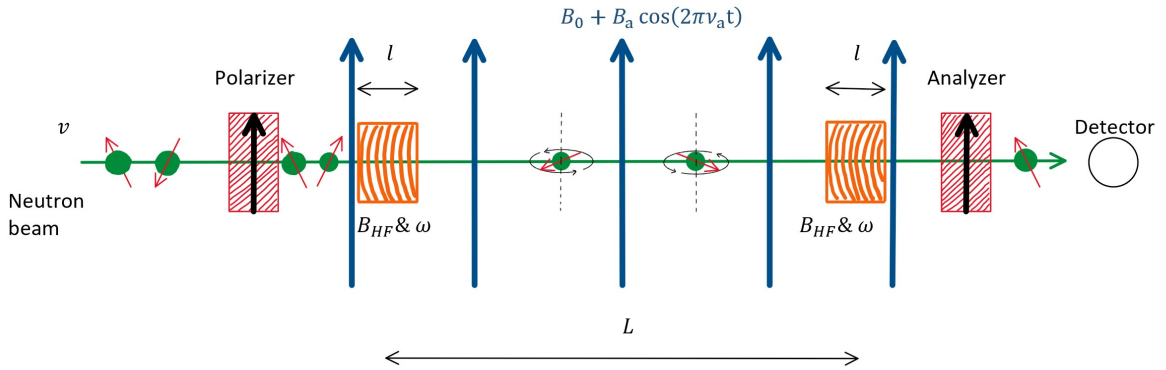


Figure 4.3: Schematic of a Ramsey setup with oscillating fields: The only difference to the classic Ramsey is the additional time dependent magnetic field  $B_a$

The justification for this modification of the classic Ramsey setup at the NARZISS [27] beamline was, that we aimed to check the feasibility of the axion gluon coupling [28] imitation. This would result into an oscillating neutron EDM as shown in Eq.(4.9), which is proportional to an oscillating magnetic field. Therefore we intended to check if the acquired phase of the neutrons is zero when the period of the oscillating magnetic field matches the interaction time, which also leads that the integral field is zero.

$$\underbrace{2.4 \cdot 10^{-16} \cdot \frac{C_G}{f_a} a_0 \cos(\omega_a t) \times E}_{\text{time dependent moment}} \propto \underbrace{\gamma_n \times B_a \sin(\omega_a t)}_{\text{time dependent field}} \quad (4.9)$$

For a monochromatic beam, the derivation can be done analytically and is presented in the next few lines. We want to know at which frequencies the neutrons phase contribution of the time dependent magnetic fields is zero.

$$\varphi_n = \omega t = -\gamma_n B t \quad (4.10)$$

Since the field is time dependent, an integration over a whole period has to be performed. Choosing the time dependent field in a way as in Eq.(4.11) will simplify the derivation.

$$\varphi_n = -\gamma_n \int B_a(t) dt; \quad B_a(t) = B_a \cos(2\pi\nu_a t) \quad (4.11)$$

$$\begin{aligned} \varphi_n &= -\gamma_n \int_0^T B_a(t) dt \\ &= -\gamma_n \int_0^T B_a \cos(2\pi\nu_a t) dt \\ &= -\gamma_n B_a \int_0^T \cos(2\pi\nu_a t) dt \end{aligned}$$

Since we want to search for the maximal amplitude of the integral, we can use symmetric integration constants because the maximum is at  $t = 0$

$$\begin{aligned} &= -\gamma_n B_a \int_{-T/2}^{T/2} \cos(2\pi\nu_a t) dt \\ &= -\gamma_n B_a \left[ \frac{1}{2\pi\nu_a} \sin(2\pi\nu_a t) \right]_{-T/2}^{T/2} \\ &= \frac{-\gamma_n B_a}{2\pi\nu_a} [\sin(\pi\nu_a T) - \sin(-\pi\nu_a T)] \\ &= \frac{-\gamma_n B_a}{\pi\nu_a} \sin(\pi\nu_a T) \\ \varphi_n^{max} &= \frac{\gamma_n B_a}{\pi\nu_a} \sin(\pi\nu_a t_{\text{int}}) \end{aligned} \quad (4.12)$$

The phase contribution has the parameters  $B_a$  for the amplitude of the time dependent magnetic field,  $\nu_a$  as the signals frequency and  $t_{\text{int}}$  as the interaction time (the time which the neutrons spend in the interaction length  $L$ ).

$$\text{roots at: } \nu_a = n \cdot \frac{v_n}{L} = n \cdot t_{\text{int}}^{-1}; \quad n \in \mathbb{N} \quad (4.13)$$

In theory, the contribution to the neutron phase should be zero, when the inverse interaction time  $t_{\text{int}}$  of the neutron matches the field's frequency  $\nu_a$ . The parameters for the interaction time are the distance between the spin flippers and the neutrons velocity.

Figure 4.4 is showing a simulation for the phase contribution to the neutrons for a fixed interaction length and different neutron velocities.

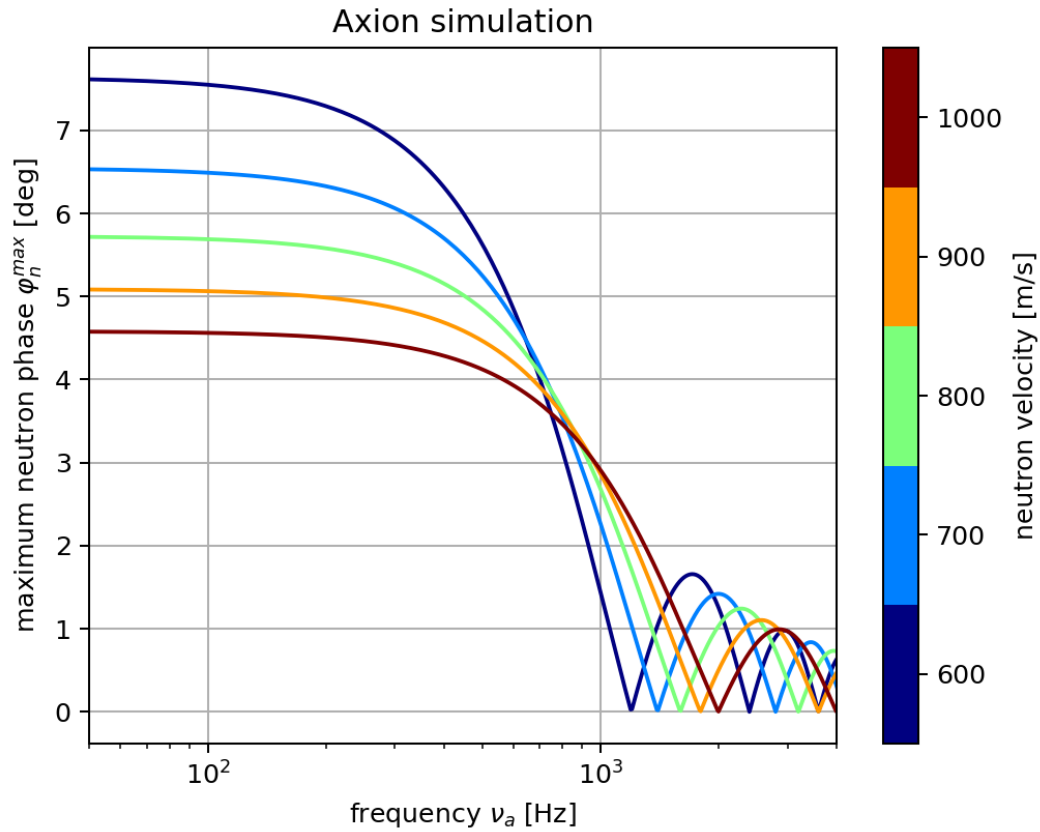


Figure 4.4: Phase behavior for different neutron velocities and at different frequencies for a fixed interaction length  $L = 0.5$  m and magnetic field amplitude  $B_a$ . The different lines, which represent neutrons with different velocities, follow Eq. (4.12)

The plot in Fig. 4.4 is also showing, whether a certain experiment is sensitive to this phase contribution or not.

# Chapter 5

## Methods

### 5.1 Preliminary measurements

Avoiding to face unexpected problems during the beam time at NARZISS, some preliminary measurements and experiments had been performed.

#### 5.1.1 Preparation in our lab

The wavelength of the neutron beam is 0.5 nm, this would lead to a velocity of the neutrons of 791 m/s with:

$$v = \frac{h}{m_n \lambda}, \quad (5.1)$$

where  $h$  is the Planck constant and  $m_n$  is the neutron's mass. With the order of 0.5 m for the interaction length, the first dip would then appear at 1600 Hz, according to Eq. ((4.13)). One issue of the measurement at NARZISS is the required high frequency of the time dependent magnetic fields. At these frequencies, the time dependent fields are shielded by the aluminium and other metallic parts of the setup. Therefore a frequency response measurement at the beamline, with the setup for creating the time dependent magnetic fields, would be necessary.

The first critical point were our fluxgates. We had to be sure they were able to measure the magnetic field at a range up to 2-3 kHz. The SENSYS FGM3D fluxgate's data sheet states a bandwidth or cut-off frequency of 2 kHz. After a private correspondence with SENSYS, every fluxgate is tested individually and the testing reports are available on request. The 1 mT fluxgate with S/N 1990 has a bandwidth above 1830 Hz for all three axes and the 250  $\mu$ T fluxgates with S/N 2003 and 2004 have an even higher bandwidth with 2620 Hz resp. 2930 Hz for all three axes. At the beam line we would operate at about 3 mT, to have a resonance frequency at around 92 kHz. But none of them would be able to measure the time dependent magnetic field while running the electromagnet. Thankfully it is not required that the electromagnet, which in fact only applies an DC offset magnetic field, is turned on while we measure the magnetic field amplitude of the sinusoidal component of the time dependent magnetic field.

Although the fluxgates with S/N 2003 and 2004 have a higher bandwidth, they are limited by a maximum amplitude of  $250 \mu\text{T}$ , whereas the fluxgate with S/N 1990 can measure up to four times higher magnetic fields. Therefore we decided to use the 1mT fluxgate with S/N 1990. For the characterization of the fluxgate we connected a Keysight



Figure 5.1: Characterization of the fluxgate inside the 3D Helmholtz coil

waveform generator (WFG) to the KEPCO bipolar operational amplifier (Model:BOP 20-20DL, S/N:E166092) and connected it to a 3D Helmholtz coil. To check the actual current, a multimeter was added. The 3D Helmholtz coil is able to produce magnetic fields in three directions. Figure 5.1 shows, that one can also choose whether to induce the magnetic fields with a copper coil or the aluminium frame of the coils for each direction. The aluminium frame coil was used since it keeps the inductance low. The fluxgate was positioned in the center of the coil, in order to have the most homogeneous field inside

of the coil. The WFG's settings were high-Z, a sinusoidal signal with an amplitude of 1 Vpp and we scanned the frequency from 1 Hz to 5 kHz.

For the analysis a Butterworth low pass filter function was used for the fitting function:

$$G = \frac{G_0}{\sqrt{1 + \left(\frac{\nu}{\nu_{\text{cut-off}}}\right)^{2n}}}, \quad (5.2)$$

where  $G_0$  is the DC gain,  $\nu_{\text{cut-off}}$  the cut-off frequency at -3 dB and  $n$  is the order of the filter. Figure 5.2 is showing the results of the frequency scan of the fluxgate inside of the 3D Helmholtz coil with its attenuation. The attenuation was fitted with Eq. (5.2), stating the cut-off frequency at around 3 kHz.

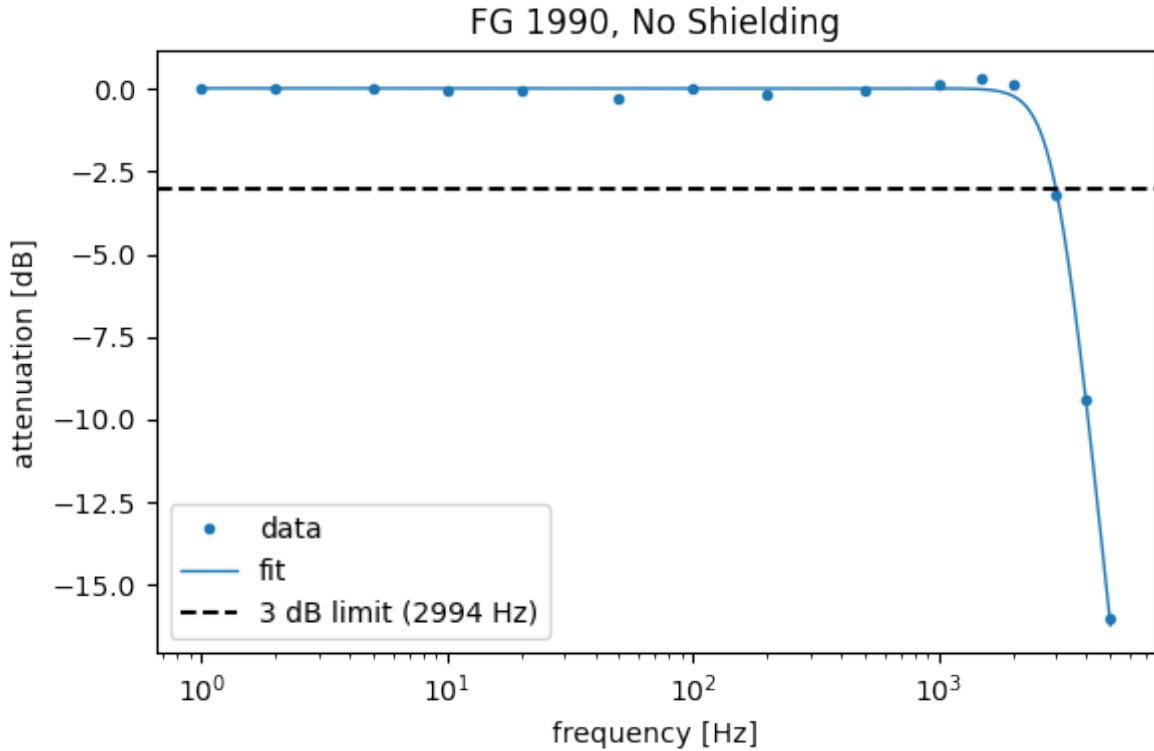


Figure 5.2: Frequency response in the Y-direction of the fluxgate S/N 1990 with a cut-off (-3 dB attenuation) frequency of about 3 kHz

As a next step the fluxgate was put into a square-shaped Helmholtz coil with a size of 76 cm x 24 cm x 12 cm. The coil that was used here was also a possible candidate to bring to the NARZISS beamline as a source for the time dependent magnetic field. The reason for this measurement was to check how strong the aluminium frame shields the oscillating fields.

To create the field with this coil we connected the Kepco amplifier to one wire of cable, which results in four windings on the top and four on the bottom side. The fluxgate



h

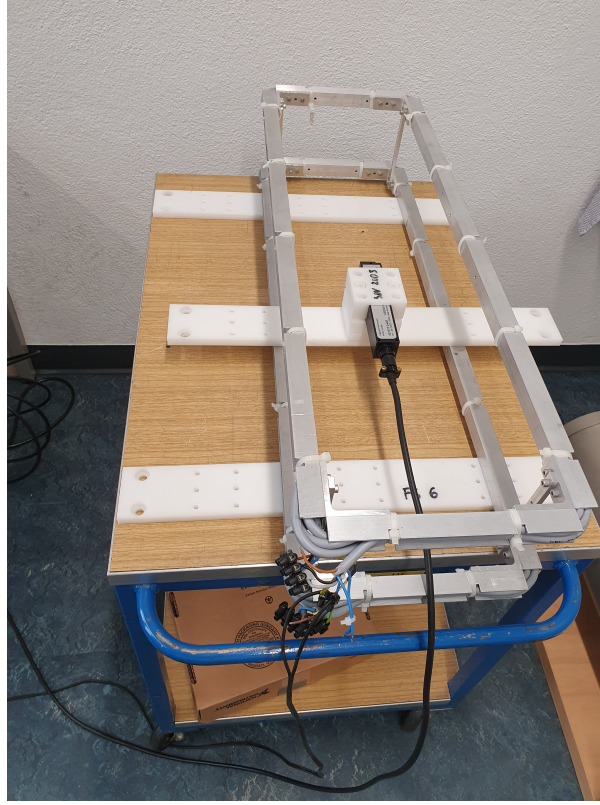


Figure 5.3: Characterization of the fluxgate inside the square shaped coil

was mounted in a way that the vertical sensor was in the very center of the coil, as visible in Fig. 5.3. The measurement was the same as for the 3D Helmholtz coil. The big difference to the first measurement was, that the coils are mounted inside of an aluminum U-profile which should shield the magnetic field at higher frequencies. Figure 5.4 shows the attenuation of the U-profile with the same fit function as in the previous plot in Fig. 5.2. In the analysis the data was divided by the attenuation of the fluxgate such that only the attenuation of the U-Profile remains. The remaining data was fitted with a Butterworth low pass filter (see Eq. (5.2)) and the filter's order was fitted to 0.9 and the 3 dB/cut-off frequency to almost 884 Hz.

At the NARZISS beamline at the PSI, the main magnetic field  $B_0$  is usually created with an electromagnet. Figure 5.5 shows how the windings of the coil are around the side of a C-shaped iron yoke. These windings produce the static magnetic field between the top and bottom plate. To check the influence of this additional iron component in the setup, the square-shaped Helmholtz coil was placed in between two iron plates, as shown in Fig. 5.6. Following the modification of our test setup, the same frequency response measurement as before was performed again.

The fit of the Butterworth low pass filter function over the measurement with the iron plates does not provide any good results. Neither in the case with the full attenuation, nor when we divided by the shielding of the fluxgate, the U-profiles or both together.

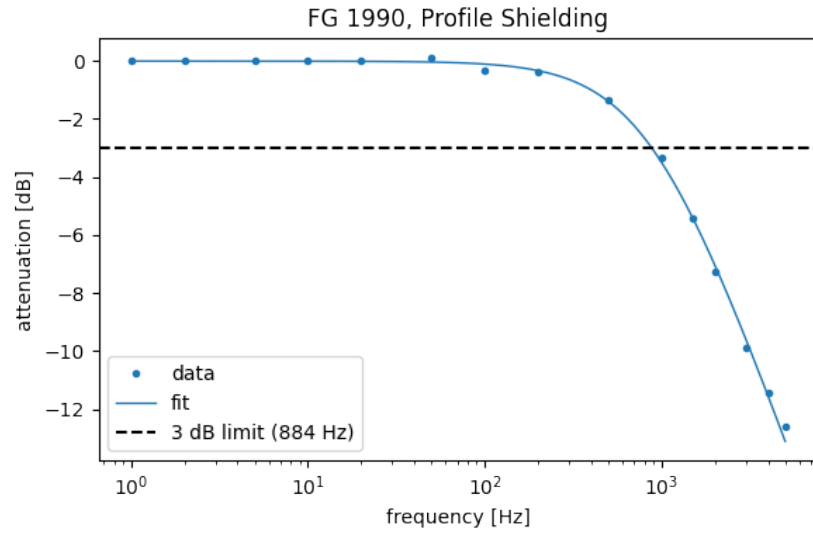


Figure 5.4: Frequency response with the aluminum U-profile with a much lower cut-off frequency of around 900 Hz

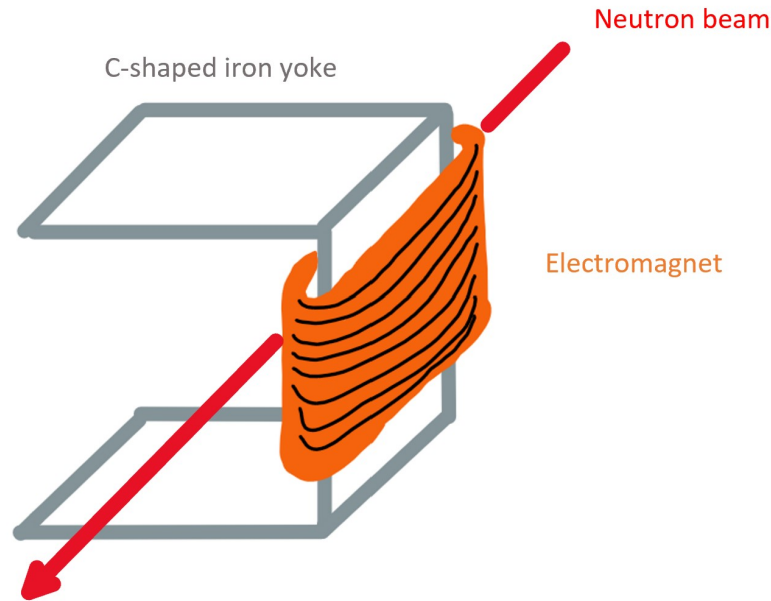


Figure 5.5: Simple sketch of the situation at the NARZISS beamline with the electromagnet wound around the C-shaped iron yoke

Therefore we show in Fig. 5.7 the full result of all the three measurements, each corresponding to one single setup. In the case for the no perturbations of the magnetic fields, coming from either aluminium or iron, the -3 dB cut-off frequency is at around 3 kHz. If the square-shaped Helmholtz coil was used for the generation of the time dependent magnetic field, its aluminium U-profiles would attenuate the signal at the higher frequen-



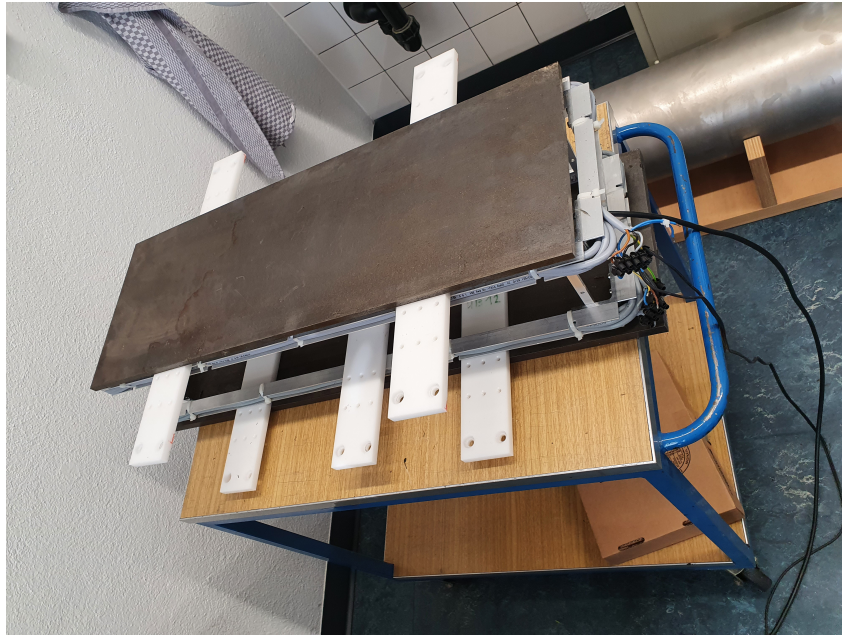


Figure 5.6: Characterization of the fluxgate inside the simulated NARZISS shielding

cies, causing the -3 dB cut-off frequency to lie around 1 kHz. For the overall setup, which consists of the aluminium U-profiles and the iron plates on top and below the square-shaped Helmholtz coil, the 3dB limit is at about 100 Hz. At 2 kHz the attenuation is -16 dB that corresponds to a shielding factor of about 6.3, at 3 kHz the attenuation is -22 dB which corresponds to a shielding factor of 12.6.

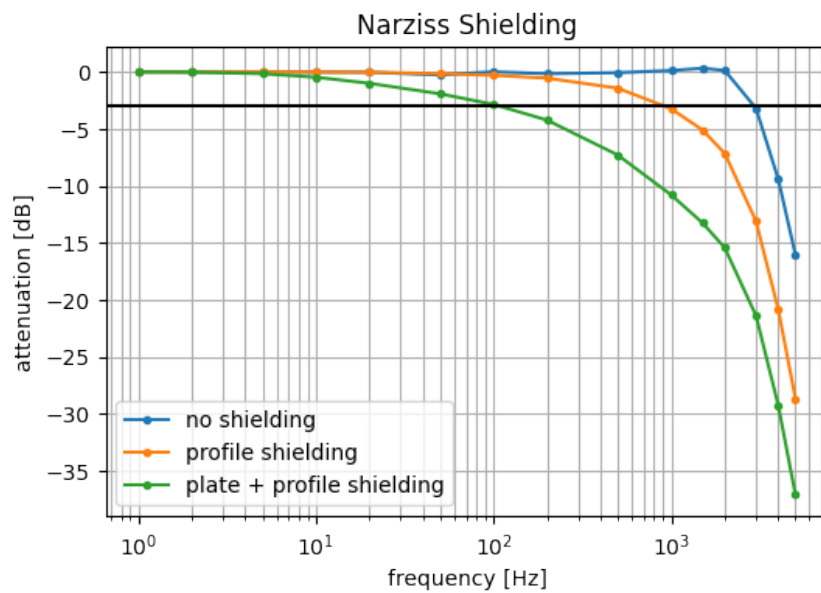


Figure 5.7: Frequency response of all three configurations

In regards to the results, we are in principle able to create an measurable oscillating magnetic field. The WFG was set to an amplitude of 1 Vpp, where the maximum would be 20 Vpp. At some point the amplifier will saturate but we tested it until 10 Vpp and no saturation occurred. This behavior has to be measured at PSI first to check the behavior in the real setup including the iron yoke of the NARZISS beamline.

### 5.1.2 Beamline at NARZISS

The beamline provides a monochromatic cold neutron beam with a wavelength of 0.5 nm which exits from the left side of Fig. 5.8 and travels to the right. There are four apertures in total to define the allowed divergence. The first one is placed directly at the beam entry to the beamline. The second and third surround spin flippers. The fourth and last aperture is placed right in front of the  $^3\text{He}$  Detector.

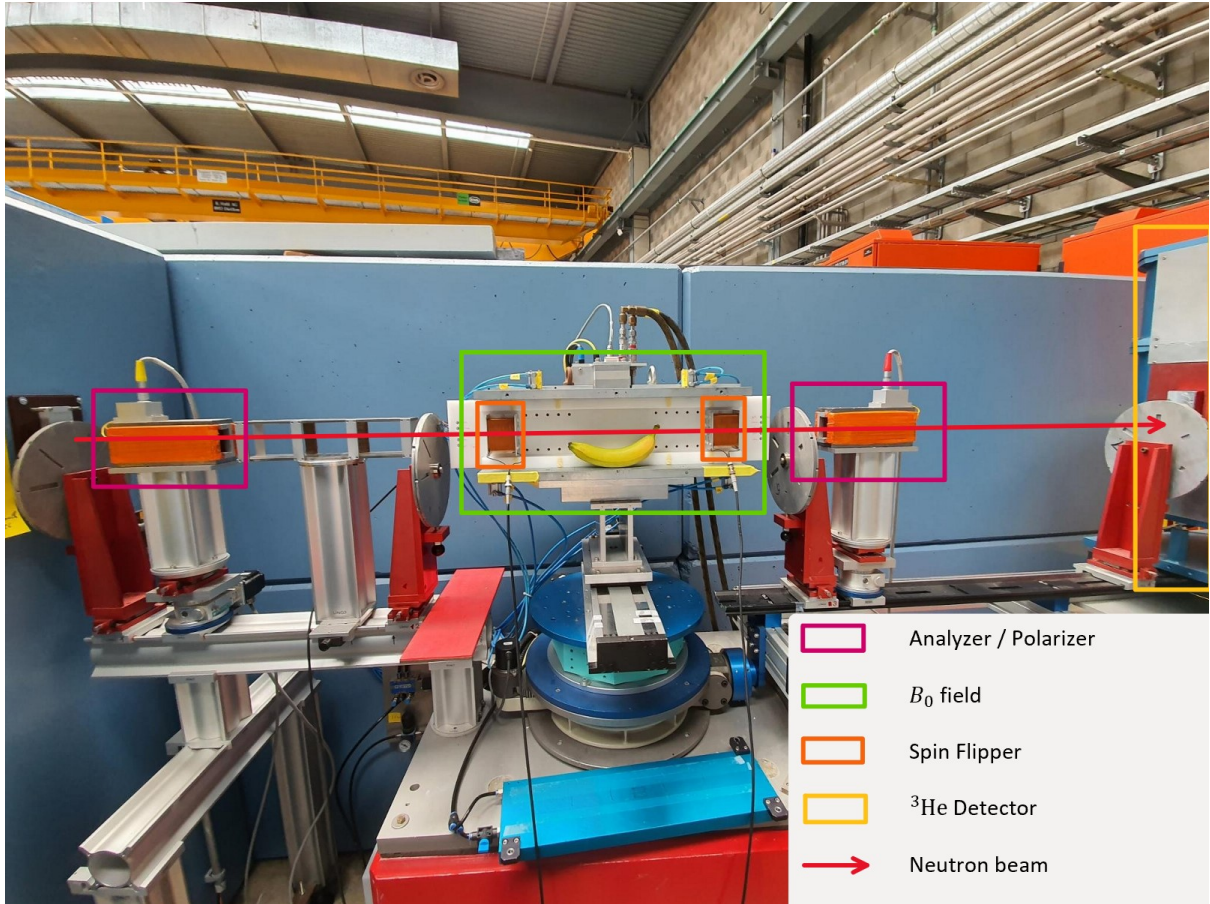


Figure 5.8: Picture of the NARZISS beamline

After the first aperture, the beam is passing through the polarizer. The polarizer at the NARZISS beamline has a silicon/iron wafer surrounded by a coil which induces a high magnetic field. Only one spin state will pass through the polarizer, while the other one will be reflected. Between the polarizer and the second aperture there is a guiding field,

made of permanent magnets, to maintain the neutrons polarization until they reach the first resonance spin flipper.

Reaching the first spin flipper, the neutrons will do their first  $\pi/2$  flip, precessing with the Larmor frequency through the free precession area and being flipped again with a  $\pi/2$  flip at the second spin flipper. Both spin flippers and the free precession zone are in front of an electromagnet. The electromagnet lies behind the spin flipper's holder (Fig.5.8) and is responsible for the  $B_0$ -field, which is needed for the Rabi/Ramsey setup.

Leaving the magnetic field of the electromagnet, the beam now has to pass the analyzer, which is similarly separating the two spin states in the same manner as the polarizer. Therefore only neutrons with the spin up state will reach the detector.

Additional to the detector counts the number of neutrons entering the beamline are also monitored. This is useful if one wants to normalize the neutron detector counts, since the flux of neutrons from the SINQ source is not stable.

### 5.1.3 Test measurements at NARZISS

The goal of the test measurements was to get familiar with the NARZISS beam line at PSI. Especially with the electro-magnet, which creates the main magnetic field  $B_0$ . An additional idea was, instead of adding the square-shaped Helmholtz type coil in the Ramsey area, to wind some additional coil around the electro-magnet and induce the oscillating field the same way as the permanent  $B_0$  field is created. With this configuration we would not need to install additional equipment and probably the attenuation due to the aluminum U-profiles would be not existent since there are no aluminium profiles. This single winding was connected to a WFG via the Kepco amplifier to create oscillating magnetic field that we used to create the oscillating signals. Additionally we measured the neutron rate for various aperture openings.

On Fig. 5.9 and 5.10 the main part of the beamline is visible. The 1 mT ranged fluxgate from the company SENSYS was mounted in that way, that the vertical sensor is centered between the iron yoke in all three directions. The main, constant and homogeneous magnetic field is created by the electromagnet with its copper coils and lies in between the iron plates. The single green additional winding around the copper coils (Fig. 5.10) was attached to create the oscillating magnetic field. It is positioned vertically centered on the copper coils.

To generate the oscillating field with the single winding, the WFG, set to a sinusoidal signal, high Z, zero offset and zero phase shift, was connected to a current programming input of the Kepco amplifier. Then we connected the amplifier to the green coil as in Fig. 5.10. The fluxgate was connected to its breakout box and from there we connected all three signals, one for each direction, to a Teledyne Lecroy oscilloscope (Model:HDO4024A, S/N: LCRY3516N52545). The oscilloscope was set in AC-coupling mode and the signal amplitude was measured with the internal measure option of the oscilloscope. As already mentioned, all three directions of the fluxgate were tracked, but only to ensure a proper alignment inside of the oscillating magnetic field. Only the vertical component was measured.



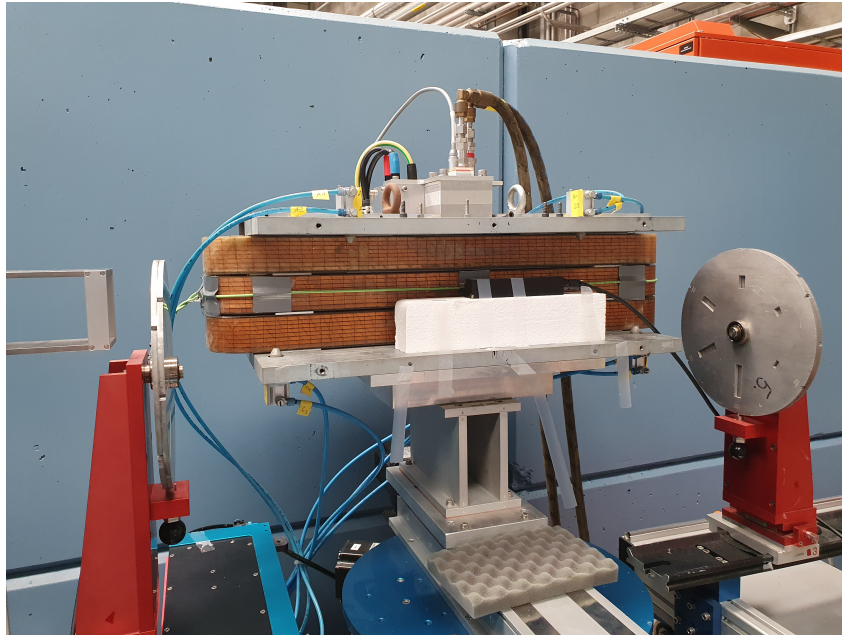


Figure 5.9: Position of the Sensys fluxgate from the front

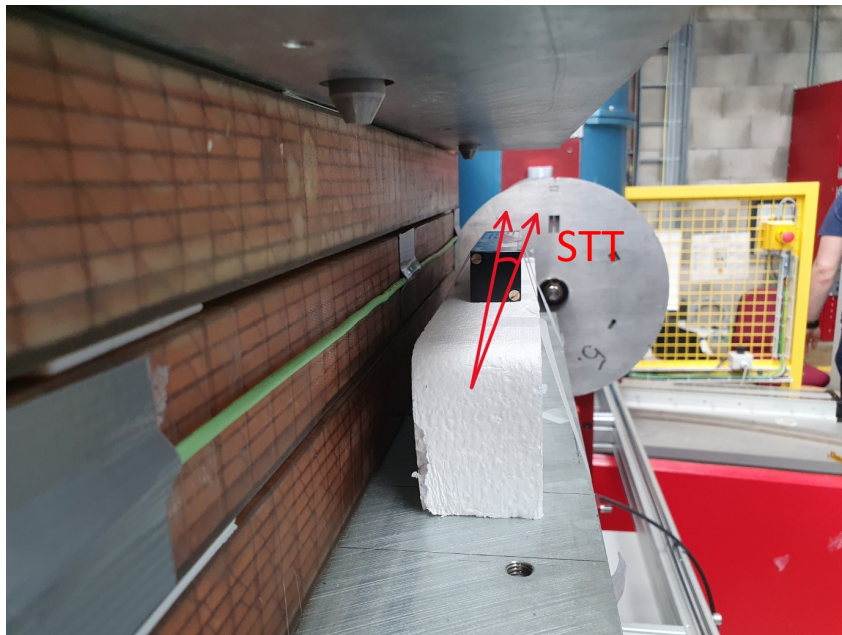


Figure 5.10: Position of the Sensys fluxgate from the side

The neutrons are detected with the  $^3\text{He}$  detector from the NARZISS beam line. The position or angle of the detector has one degree of freedom, the detector angle with respect to the center of the interaction zone in transversal direction, which is called STT. To measure the neutron rate this position has to be optimized with respect to the neutron beam. To do so the aperture size of the fourth aperture  $A_4$  was reduced to  $30 \times 0.2 \text{ mm}^2$ .



Figure 5.11: Detector Position: The neutron counts at the detector are normalized with 200 k monitor counts

The previous apertures were set to a size of  $30 \times 1 \text{ mm}^2$ . Figure 5.11 shows that the optimal position is at about 0.02 deg which is a slight offset from the zero reference.

With  $\text{STT} = 0.03 \text{ deg}$  set as the detector position, a value that we agreed to use since without having done the analysis like in Fig. 5.11 the value of 0.03 deg appeared to be the "maximum by eye", we measured the neutron rate for 10 seconds. The rates were measured for aperture heights of 20 mm and 30 mm, as well as widths of 1 mm and 2 mm. These aperture sizes are the reasonable ones for our measurement. All four apertures were set to the same heights and widths and the measurements were again performed for 10 seconds and all were normalized with the monitor count (Fig. 5.12). The expectation was a quadratic behavior of the neutron counts with an increment of the aperture size, which was confirmed by the measurements.

The first magnetic field test was about the single winded coil, which should create an oscillating field. The static field was turned off, otherwise the fluxgate would have saturated. The WFG was set to a frequency of  $\nu = 10 \text{ Hz}$  and the amplitudes were scanned between 1 and 15 Vpp. In Fig. 5.13. the amplitudes behaves linear as expected.

Additionally we set the WFG to 10 Vpp and turned on the static magnetic field created by the electromagnet. Then we scanned the magnetic field amplitude of  $B_0$  from the electromagnet to check whether the oscillating amplitude is constant for different  $B_0$  fields or not

According to Fig. 5.14, the oscillating magnetic field amplitude seems to be more or less constant for all  $B_0$  values within the error of the measurement.

In the end of our test beamtime at NARZISS we fixed the amplitude on the WFG to 10 Vpp and scanned the frequency from 1 to 5000 Hz (Fig. 5.15).

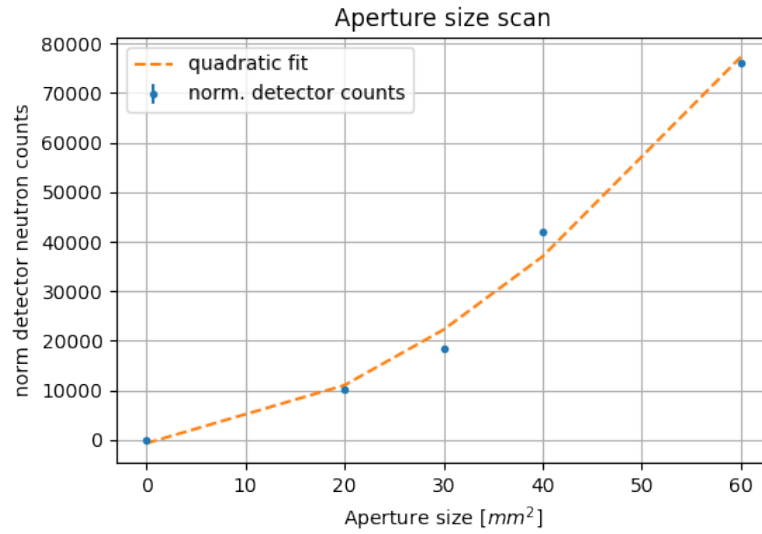


Figure 5.12: Aperture size

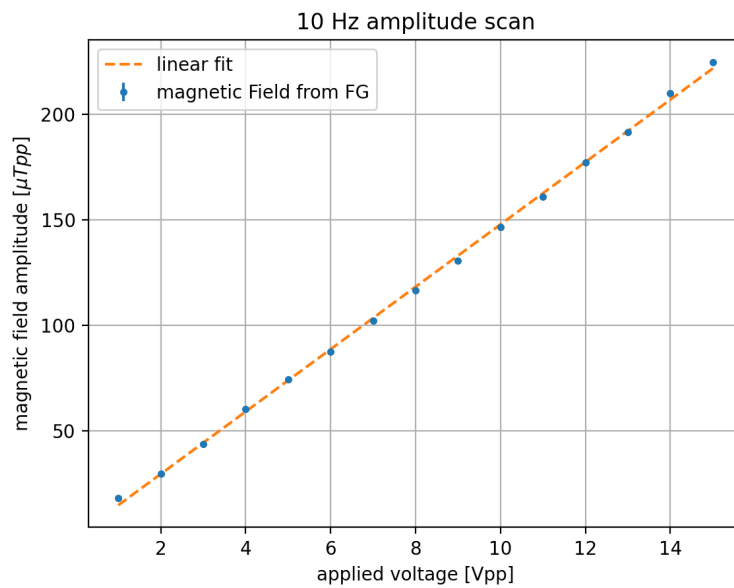


Figure 5.13: Amplitude scan

This measurement shows at the lower frequencies firstly a linear increase, then a linear decrease. Above 50 Hz, a flat plateau occurs with a sharp cut-off at frequencies higher than 2500 Hz. In the range between 1 and 50 Hz, the behavior not be explained at that moment. One possible reason could be the frequency response of the amplifier or some effects of the iron yoke and the copper coils which would need some further investigation. Since the frequencies below 50 Hz are not interesting for our time dependent magnetic field measurements, this seemed not very important.

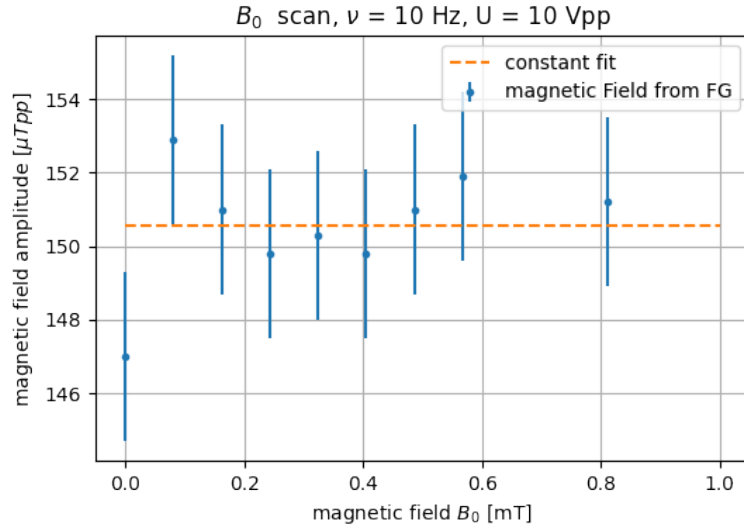
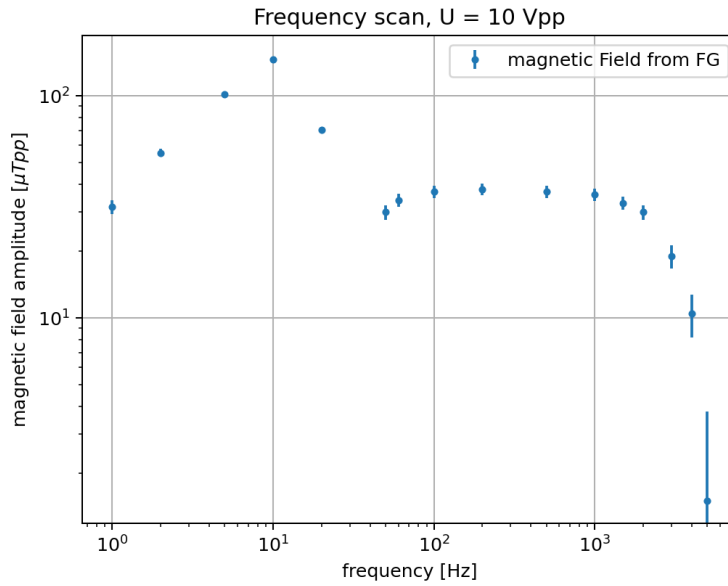
Figure 5.14:  $B_a$  amplitude for various values of  $B_0$ 

Figure 5.15: Frequency scan of the time dependent magnetic field source

The data of the region of interest for our future measurements is presented in Fig. 5.16 with a least-squares fit of a low order Butterworth low-pass filter function (see Eq. (5.2)). Without the subtraction of the frequency response Fig. 5.7, the 3 dB limit is fitted to be at 2419 Hz. Since the first dip is expected at about 1600 Hz and the second one at 3200 Hz (Eq. (4.13)), the measurements with oscillating magnetic fields at the NARZISS beamline seemed feasible.

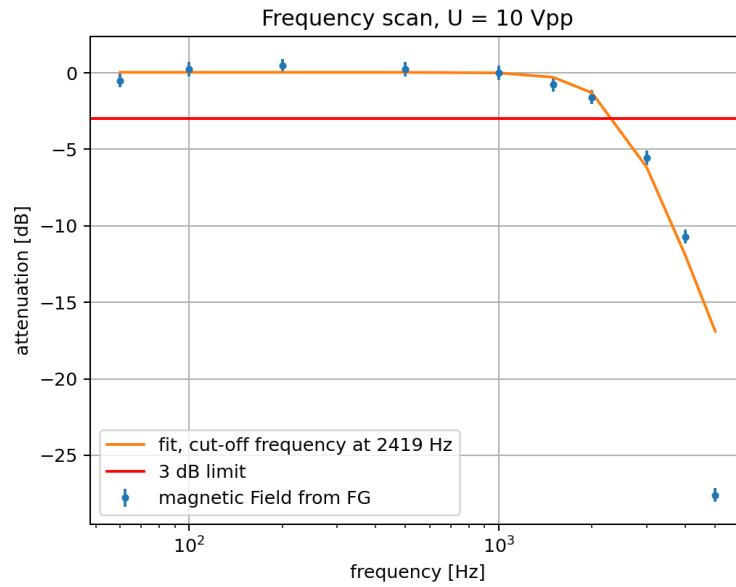


Figure 5.16: Frequency scan of the region of interest

## 5.2 Experimental procedure

For the production of the oscillating signals, a holder was made of POM which included five stripes of aluminum and was also used as a holder for mounting the spin flippers on. The holders are visible in Fig. 5.17.

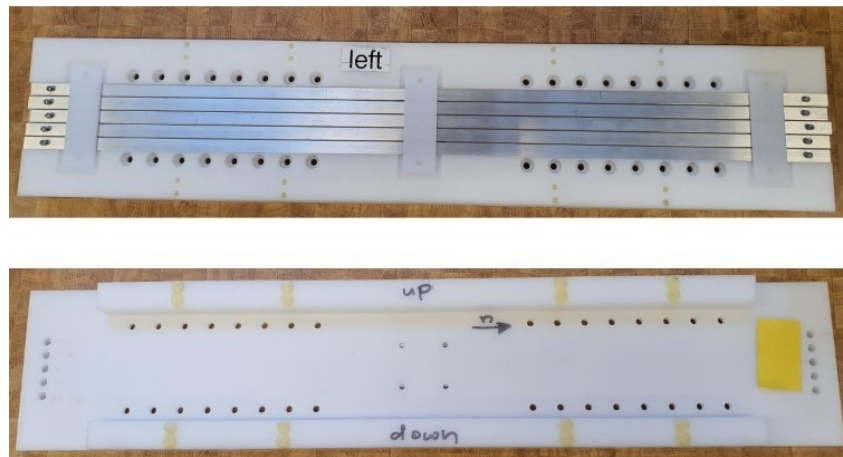


Figure 5.17: Holder for the spin flippers, made of POM. The upper picture is showing the backside with the aluminium stripes, which create the oscillating magnetic fields. The lower picture is showing the frontside, with threads for the fixation of the spin flippers.

It was designed in a way, that it fitted perfectly inside of the iron yoke of the NARZISS beam line, which is visible in Fig. 5.8. The aluminum stripes were connected in series



around the sampling magnet, to create the oscillating magnetic fields.

Before starting the measurements, the beam line had to be set up properly. The four apertures were set to  $30 \times 1 \text{ mm}^2$  to align the analyzer with a laser pointer. The laser beam was going through A2 - A4 and into the detector, before the analyzer was mounted. When all the angles of the beamline were in line, the analyzer was added just after A3 and aligned in the transversal position by hand to see the laser pointer in the center of the wafers. Then the apertures were set back to  $30 \times 2 \text{ mm}^2$ .

With a Hall probe the vertical magnetic field at the position of the spin flippers was measured. We increased the current for the sampling magnet (SMAG) until we reached a magnetic field shown from the Hall probe of 3.15 mT, which corresponds to the resonance frequency of 92 kHz.

Settings for the SICS/NARZISS were:

- POM 0.8 (Angle of the polarizer)
- PMAG 1 (Current for the magnetic field at the polarizer)
- SOM 0 (Angle of the interaction zone)
- STY -51.5 (Horizontal position for the interaction zone)
- SMAG 3.9 (Current for the sampling magnet)
- AOM 0.1 (Angle of the analyzer)
- AMAG 1 (Current for the magnetic field at the analyzer)
- STT 0.02 (Angle of the detector with respect to the center of the interaction zone)
- all apertures at  $30 \times 2 \text{ mm}^2$

The installation of the spin flipper holder was very simple. Firstly both spin flippers were centered with a distance of 50 cm between each on the holding. The holder was secured by bolts of the apparatus at the NARZISS beamline.

For both of the spin flippers, a Rabi frequency scan and amplitude scan were performed. As described in Sec. 4.2.1, for a Rabi frequency or amplitude scan only one spin flipper needs to be operated. Both measurements were executed on both spin flippers separately, to also check if they behave in the same way.

The Rabi frequency scan will give the resonance frequency, at which the spin flipper has to be operated in general. In Fig. 5.18 such a Rabi frequency scan is shown. The minimum of this performed measurement is located for the left spin flipper and the right spin flipper at  $(91.854 \pm 0.003) \text{ kHz}$  and at  $(91.414 \pm 0.004) \text{ kHz}$ .

Instead of scanning the frequency, also the amplitude of the signal going through the spin flipper can be scanned. For this measurement the resonance frequency from the Rabi frequency scan is used. We fix this frequency while we scan the amplitude as presented in Fig. 5.19. The minimum of the neutron counts will show the right amplitude, where a

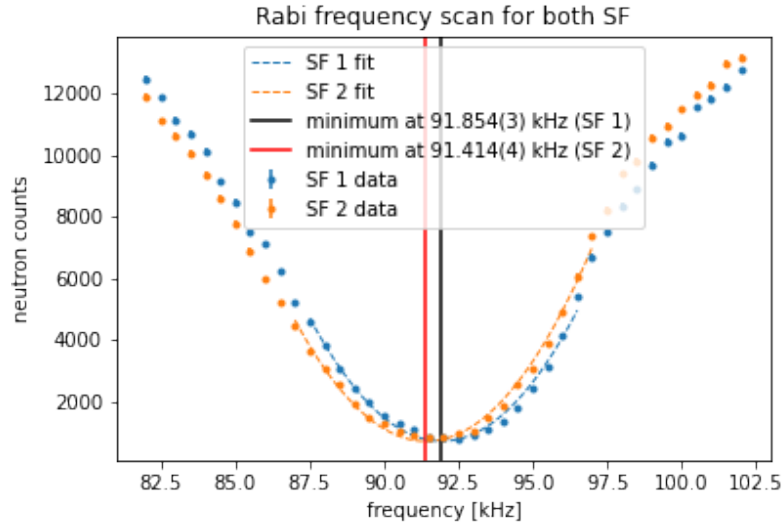


Figure 5.18: Rabi frequency scan for both spin flipper

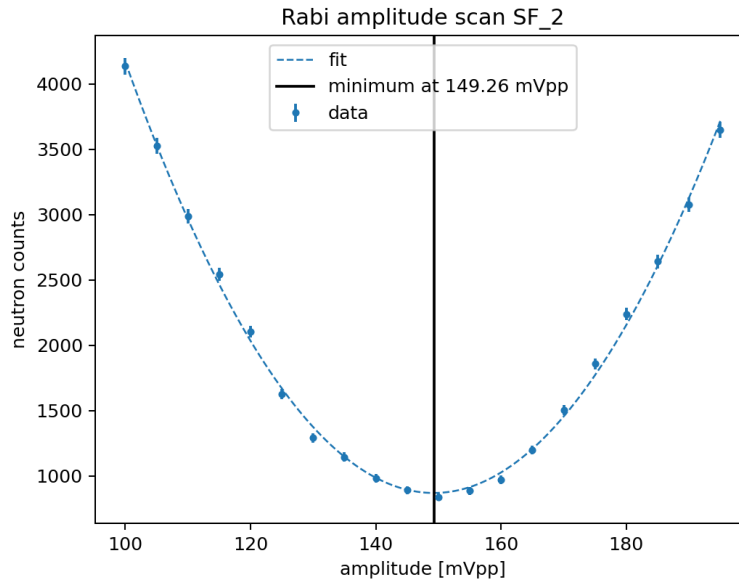


Figure 5.19: Rabi amplitude scan of the right spin flipper

full  $\pi$  flip of the neutrons is performed. Dividing the amplitude in half should therefore also result in a  $\pi/2$  flip for each spin flipper.

Performing both, the Rabi frequency scan and Rabi amplitude scan on both spin flippers, we decided to use the same amplitude of  $A = 74$  mVpp and the average resonance frequency of  $\nu = 91.700$  kHz for the following Ramsey measurements.

For the Ramsey measurements both spin flippers were now active. Firstly, a phase scan has been performed. For this, both frequencies and both amplitudes were set to the values

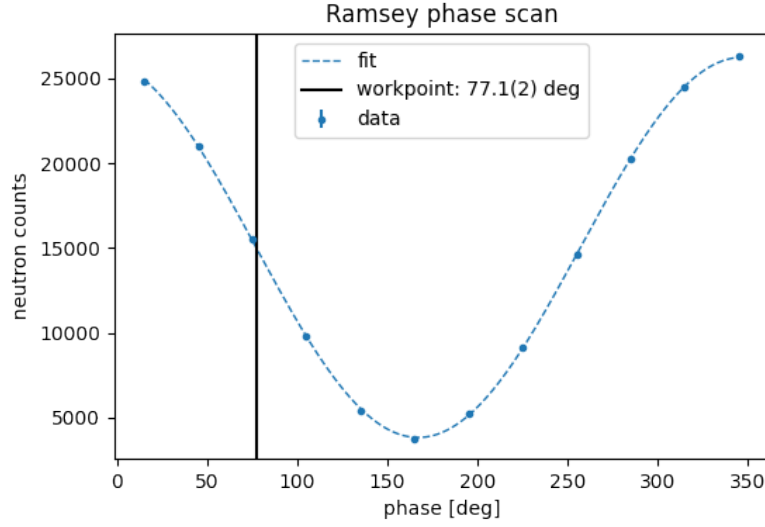


Figure 5.20: Ramsey phase scan in steps of 30 deg, with a phase of  $-102,9(2)$  and the working point at  $77.1(2)$  deg

obtained from the Rabi measurements. Only the phase of the second spin flipper was now scanned to find the working point. A good working point is at the most linear regime of the phase scan. With a least squares fit the phase was obtained from a sinusoidal fitting function and by adding 180 deg one gets the working point to be at the linear falling of the sinusoidal function as shown in Fig. 5.20.

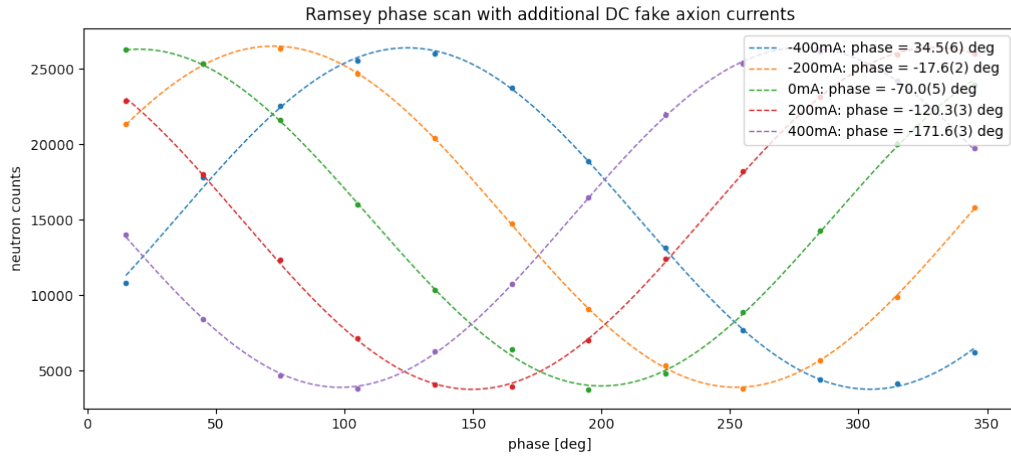


Figure 5.21: Ramsey phase scan with DC currents on the source for the later oscillating magnetic fields

Putting different DC on the source for the time dependent magnetic field at the spin flipper holdings would change the static magnetic field  $B_0$  of the sampling magnet, which leads to different precession frequencies of the neutron. Performing a phase scan with

the second spin flipper (right SF in Fig. 5.8) results for each DC setting in a phase shift. In Fig. 5.21 one can review the nice frequency shifts of various currents. A difference of 200 mA resulted in a 50 deg phase shift (0.25 deg/mA), as we expected it to behave. The measurement with the DC signals was nothing more than a test to see, how the source for the oscillating field  $B_a$  works. Since we want to apply the oscillating fields, we were more interested in the neutrons reactions to additional AC fields next to the static  $B_0$  field in the free precession zone.

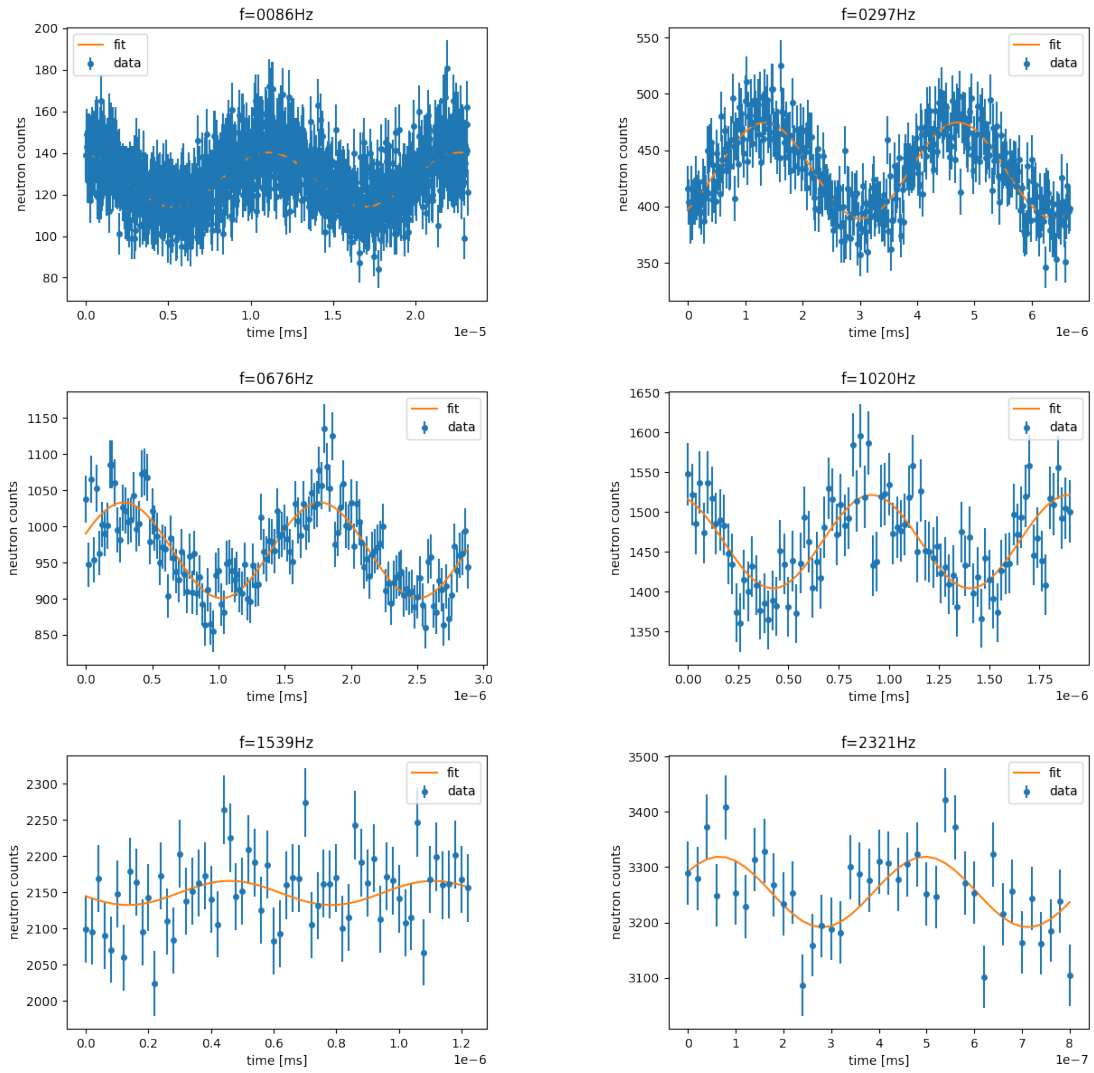


Figure 5.22: Single measurements of the fine scan at different frequencies, showing the oscillating neutron counts with its fitted amplitude

The expectation was, that the neutron's phase would start to oscillate when applying the oscillating magnetic field  $B_a$  as described by Eq. (4.12) and also by the Fig. 4.4. Having the spin flippers at a working point in the most linear regime as it is shown in Fig. 5.20, also the neutron counts are expected to oscillate.

Knowing only the integrated number of neutrons entering the beamline (monitor counts) and entering the detector (detector counts) was insufficient. For the measurements with the time dependent field also time bins were added in order to know how many neutrons enter the detector at which time. We measured the neutron counts as a function of the time and swept the data into two periods. The dwell time (time bin size) was set to  $20 \mu\text{s}$ . The signals for the source of the oscillating field were programmed for a frequency scan from 60 to 3500 Hz in 99 logarithmic steps for the frequency of the oscillating field  $B_a$ . The data acquisition (DAQ) was set to finish one measurement, when the monitor counts reaches  $2 \cdot 10^6$  counts and when the measurements exceeds the measurement time of 10 seconds to have enough data for the analysis, then to switch the frequency of the WFG to the next value and to start the next measurement. This process was repeated three times through the night. In Fig. 5.22 a single measurement iteration of the neutron signals for oscillating fields at various frequencies is shown. Approaching the frequency, where the phase contribution disappears, the amplitude of the neutron counts decreases. Past this frequency, the amplitude rises again.

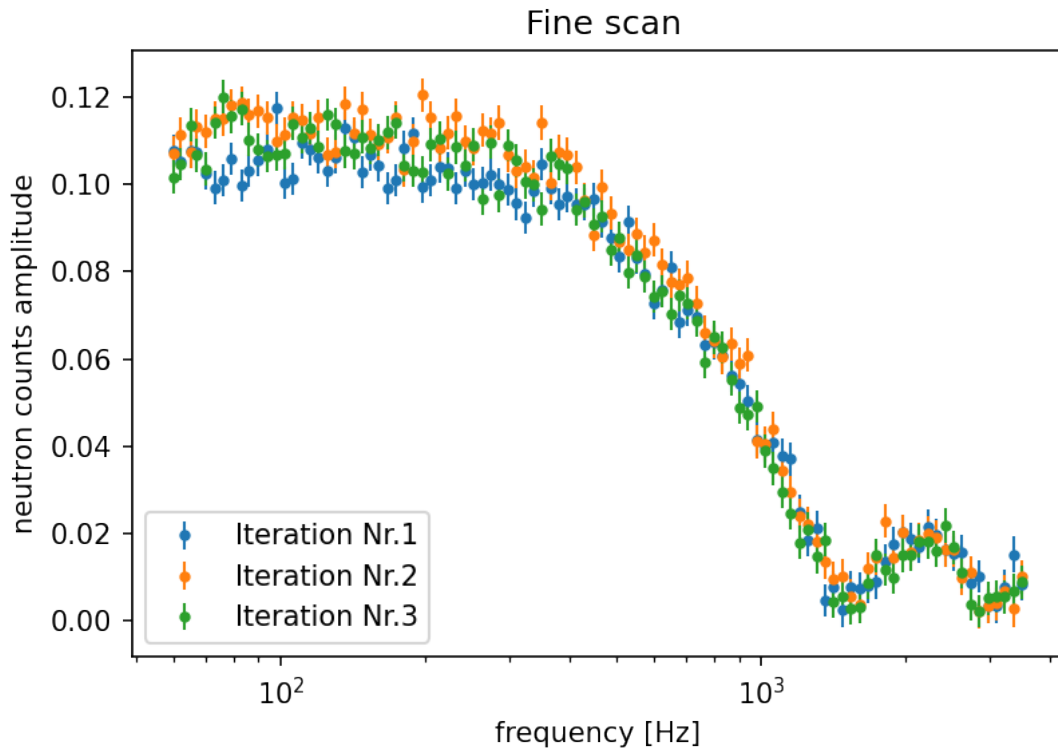


Figure 5.23: Neutron count amplitudes of the fine scan with all three iterations

Subsequently the amplitudes of the neutron count oscillations were fitted with the function from Eq. (4.12) with fixed frequencies as in Fig. 5.22 for all frequencies and for all iterations and were added to one plot, to see if the measurements were performed without any problems. Figure 5.23 shows fitted neutron count amplitudes of all three iterations.

# Chapter 6

## Results and discussion

The main result is the behavior of the neutron count's amplitude at different frequencies. As described in Sec. 4.3, the expectation was that the oscillation's amplitude goes to zero if the period of the oscillating signal  $\nu_a^{-1}$  matches the interaction time.

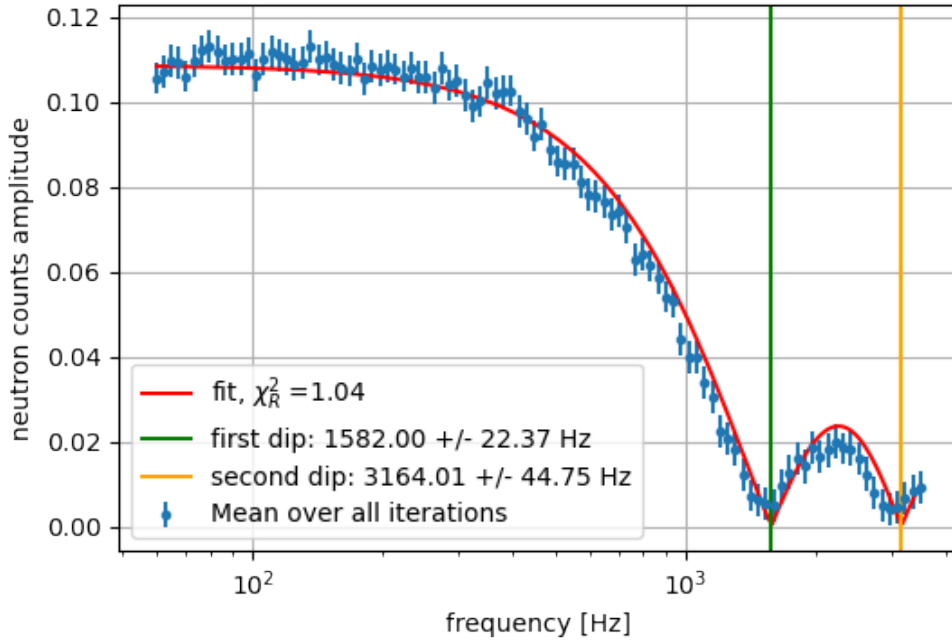


Figure 6.1: Mean neutron count amplitude of the fine scan with the fitted function and the marked roots of the fitted function from Eq. (4.12)

The mean signal of the three iterations from the fine scan has been fitted with the function in Eq. (4.12), with  $B_a$  as the fitting parameter and with fixed frequencies  $\nu_a$ . From this fit we extracted the dips (which are the roots of the fitting function) and compared the frequencies of the first and second dip to the expected values from Eq. (4.13). The fitting function is suggesting a frequency of 1582 +/- 22.37 Hz and 3164 +/- 44.75 Hz for the first

dip and for the second dip, respectively. According to Eq. (4.13), with an interaction time of  $6.32 \cdot 10^{-4}$  s (neutron velocity of 791 m/s and a interaction distance of 0.5 m) the first and the second dip is predicted at 1600 Hz and 3200 Hz, respectively. The  $\chi_R^2$  value of 1.04 states, that the fit with the one fitting parameter  $B_a$  matches the data. The measured roots match also to the expected root values, taking the errors into account. In the fitting function from Eq. (4.12) also the interaction time  $t_{\text{int}}$  could be used as a fitting parameter. Since our  $\chi_R^2$  value is already quite close to one, adding an additional parameter should bring the  $\chi_R^2$  value below one, indicating an overfitting. This is exactly what happened, shown in Fig. 6.2. Not only the  $\chi_R^2$  value changed drastically, also the position for the dips has changed. By giving additionally the interaction time  $t_{\text{int}}$  as a second fitting parameter, the fitted dips appear at lower frequencies, than in Fig. 6.1. Namely at  $1419 \pm 7.17$  Hz the first dip appears respectively at  $2988 \pm 14.35$  Hz for the second dip.

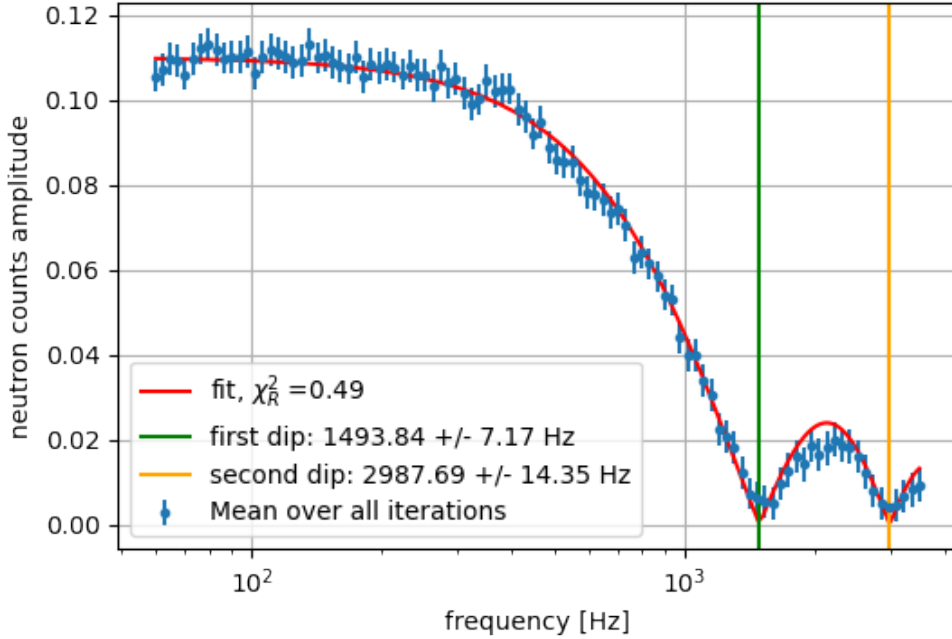


Figure 6.2: Mean neutron count amplitude of the fine scan with the fitted function, including two fitting parameters,  $B_a$  and  $t_{\text{int}}$

The distance between the spin flipper was measured to be around 0.5 m. But also the length of the spin flipper itself, according to [29], has an effect on the interaction length  $L$ , therefore also on the interaction time  $t_{\text{int}}$  in Eq. (4.13). With  $L = 47$  cm as the distance from center to center of both spin flippers and  $l = 7.5$  cm as the length of the spin flippers (see Fig. 4.2), the new interaction length scales with:

$$l_{\text{int}} = L \left( 1 + \frac{4}{\pi} \frac{l}{L} \right) = 55.9 \text{ cm} \quad (6.1)$$

With this new interaction length, also the predicted frequencies, where the dips occur will change. The first expected dip should appear at a frequency of 1413 Hz respectively 2826 Hz for the second dip. Even with this scaling of the interaction length, the values do not match as good as the first attempt with only one fitting parameter. Not only because of the worse  $\chi_R^2$  value, also the measured roots do not match as good as the ones extracted from the fitting function with only one parameter.

The imitation of the axion gluon coupling at the NARZISS beamline with our oscillating Ramsey setup was successful. We checked that the acquired neutron phase and the integral field inside the interaction length is zero and we were able to reproduce the dips at the expected frequencies at around 1600 Hz for the first dip respectively at around 3200 Hz for the second dip.

The following improvements were not taken into account during the experiment or analysis:

- Even though the beam is stated to be monochromatic with a wavelength of 0.5 nm (and a neutron velocity of 791 m/s), there could exist a slight velocity distribution around this value. This was not taken into account in the analysis and it is mentioned here as a possible improvement. As already told in Sec. 4.3, calculations and simulations assuming a pure monochromatic beam is easier than having a velocity distribution. This does not mean that simulations with a white beam have not been done.
- In the Sec. 5.1.1 and 5.1.3, the attenuation of the fluxgate (Fig. 5.7) and also the beamline with the iron yoke (Fig. 5.16) was evaluated. For the analysis, these effects were not taken into account.

For future experiments one has to pay attention when choosing the interaction time. By setting it right, one can avoid any unwanted neutron's phase contributions in the interaction zone, which can happen due to the axion gluon coupling.



# Bibliography

- [1] J Osborne et al. “Fully integrated standalone zero field optically pumped magnetometer for biomagnetism”. In: *Steep Dispersion Engineering and Opto-Atomic Precision Metrology XI*. Vol. 10548. International Society for Optics and Photonics. 2018, 105481G.
- [2] *QZFM Gen-3 – QuSpin*. URL: <http://quspin.com/products-qzfm/> (visited on 01/03/2022).
- [3] David Cohen. “Magnetic fields of the human body”. In: *Physics Today* 28.8 (Aug. 1975), pp. 34–43. ISSN: 0031-9228, 1945-0699. DOI: [10.1063/1.3069110](https://doi.org/10.1063/1.3069110). URL: <http://physicstoday.scitation.org/doi/10.1063/1.3069110> (visited on 05/26/2021).
- [4] David Cohen. “Steady fields of the body”. In: *Biomagnetism*. Springer, 1983, pp. 327–339.
- [5] Tim M. Tierney et al. “Optically pumped magnetometers: From quantum origins to multi-channel magnetoencephalography”. In: *NeuroImage* 199 (Oct. 2019), pp. 598–608. ISSN: 10538119. DOI: [10.1016/j.neuroimage.2019.05.063](https://doi.org/10.1016/j.neuroimage.2019.05.063). URL: <https://linkinghub.elsevier.com/retrieve/pii/S1053811919304550> (visited on 09/09/2021).
- [6] Reuben Benumof. “Optical pumping theory and experiments”. In: *American Journal of Physics* 33.2 (1965), pp. 151–160.
- [7] Malcolm H Levitt. *Spin dynamics: basics of nuclear magnetic resonance*. John Wiley & Sons, 2013.
- [8] *Introduction to Zero-Field Magnetometer – QuSpin*. URL: <http://quspin.com/products-qzfm-gen2-arxiv/zero-field-magnetometer-description/> (visited on 02/04/2022).
- [9] *Twinleaf — MS-2*. URL: <https://twinleaf.com/shield/MS-2/> (visited on 01/03/2022).
- [10] *FGM3D – Sensys Magnetometer*. URL: <https://sensysmagnetometer.com/products/fgm3d/> (visited on 02/04/2022).
- [11] *Magnetfeldsensor FLC3-70*. URL: <https://stefan-mayer.com/de/produkte/magnetometer-und-sensoren/magnetfeldsensor-flc3-70.html> (visited on 02/04/2022).

- [12] Keysight. *Trueform-Signal- und Funktionsgeneratoren*. Keysight. Section: Article Section. URL: <https://www.keysight.com/ch/de/products/waveform-and-function-generators/trueform-series-waveform-and-function-generators.html> (visited on 02/04/2022).
- [13] C. S. Wu et al. “Experimental Test of Parity Conservation in Beta Decay”. In: *Physical Review* 105.4 (Feb. 15, 1957). Publisher: American Physical Society, pp. 1413–1415. DOI: [10.1103/PhysRev.105.1413](https://doi.org/10.1103/PhysRev.105.1413). URL: <https://link.aps.org/doi/10.1103/PhysRev.105.1413> (visited on 11/02/2021).
- [14] J. H. Christenson et al. “Evidence for the  $2\pi$  Decay of the  $K_2^0$  Meson”. In: *Physical Review Letters* 13.4 (July 27, 1964). Publisher: American Physical Society, pp. 138–140. DOI: [10.1103/PhysRevLett.13.138](https://doi.org/10.1103/PhysRevLett.13.138). URL: <https://link.aps.org/doi/10.1103/PhysRevLett.13.138> (visited on 11/02/2021).
- [15] W. Pauli et al. “Niels Bohr and the Development of Physics: Essays Dedicated to Niels Bohr on the Occasion of his Seventieth Birthday”. In: *Physics Today* 9.8 (Aug. 1, 1956). Publisher: American Institute of Physics, pp. 32–32. ISSN: 0031-9228. DOI: [10.1063/1.3060063](https://doi.org/10.1063/1.3060063). URL: <https://physicstoday.scitation.org/doi/10.1063/1.3060063> (visited on 11/02/2021).
- [16] Alan Kostelecky. “The Status of CPT”. In: *arXiv:hep-ph/9810365* (Oct. 14, 1998). arXiv: [hep-ph/9810365](https://arxiv.org/abs/hep-ph/9810365). URL: <http://arxiv.org/abs/hep-ph/9810365> (visited on 11/02/2021).
- [17] M. Pospelov and A. Ritz. “Theta-Induced Electric Dipole Moment of the Neutron via QCD Sum Rules”. In: *Physical Review Letters* 83.13 (Sept. 27, 1999), pp. 2526–2529. ISSN: 0031-9007, 1079-7114. DOI: [10.1103/PhysRevLett.83.2526](https://doi.org/10.1103/PhysRevLett.83.2526). arXiv: [hep-ph/9904483](https://arxiv.org/abs/hep-ph/9904483). URL: <http://arxiv.org/abs/hep-ph/9904483> (visited on 06/24/2021).
- [18] A D Sakharov. “Violation of  $CP$  in variance,  $C$  asymmetry, and baryon asymmetry of the universe”. In: (1991), p. 3.
- [19] Michael Dine and Alexander Kusenko. “Origin of the matter-antimatter asymmetry”. In: *Reviews of Modern Physics* 76.1 (Dec. 16, 2003). Publisher: American Physical Society, pp. 1–30. DOI: [10.1103/RevModPhys.76.1](https://doi.org/10.1103/RevModPhys.76.1). URL: <https://link.aps.org/doi/10.1103/RevModPhys.76.1> (visited on 11/02/2021).
- [20] P. Schmidt-Wellenburg. “The quest for an electric dipole moment of the neutron”. In: *AIP Conference Proceedings* 1753.1 (July 7, 2016). Publisher: American Institute of Physics, p. 060002. ISSN: 0094-243X. DOI: [10.1063/1.4955363](https://doi.org/10.1063/1.4955363). URL: <https://aip.scitation.org/doi/abs/10.1063/1.4955363> (visited on 11/02/2021).
- [21] Alessandro Bettini. *Introduction to Elementary Particle Physics*. Google-Books-ID: bV2tAgAAQBAJ. Cambridge University Press, Feb. 13, 2014. 493 pp. ISBN: 978-1-107-05040-2.

- [22] C. Abel et al. “Measurement of the Permanent Electric Dipole Moment of the Neutron”. In: *Physical Review Letters* 124.8 (Feb. 28, 2020). Publisher: American Physical Society, p. 081803. DOI: [10.1103/PhysRevLett.124.081803](https://link.aps.org/doi/10.1103/PhysRevLett.124.081803). URL: <https://link.aps.org/doi/10.1103/PhysRevLett.124.081803> (visited on 11/02/2021).
- [23] R. D. Peccei and Helen R. Quinn. “ $CP$  Conservation in the Presence of Pseudoparticles”. In: *Physical Review Letters* 38.25 (June 20, 1977). Publisher: American Physical Society, pp. 1440–1443. DOI: [10.1103/PhysRevLett.38.1440](https://link.aps.org/doi/10.1103/PhysRevLett.38.1440). URL: <https://link.aps.org/doi/10.1103/PhysRevLett.38.1440> (visited on 11/02/2021).
- [24] I. I. Rabi et al. “The Molecular Beam Resonance Method for Measuring Nuclear Magnetic Moments. The Magnetic Moments of  ${}^6_3\text{Li}$ ,  ${}^7_3\text{Li}$  and  ${}^{19}_9\text{F}$ ”. In: *Physical Review* 55.6 (Mar. 15, 1939). Publisher: American Physical Society, pp. 526–535. DOI: [10.1103/PhysRev.55.526](https://link.aps.org/doi/10.1103/PhysRev.55.526). URL: <https://link.aps.org/doi/10.1103/PhysRev.55.526> (visited on 11/01/2021).
- [25] I. I. Rabi et al. “A New Method of Measuring Nuclear Magnetic Moment”. In: *Physical Review* 53.4 (Feb. 15, 1938). Publisher: American Physical Society, pp. 318–318. DOI: [10.1103/PhysRev.53.318](https://link.aps.org/doi/10.1103/PhysRev.53.318). URL: <https://link.aps.org/doi/10.1103/PhysRev.53.318> (visited on 11/01/2021).
- [26] Norman F. Ramsey. “A Molecular Beam Resonance Method with Separated Oscillating Fields”. In: *Physical Review* 78.6 (June 15, 1950). Publisher: American Physical Society, pp. 695–699. DOI: [10.1103/PhysRev.78.695](https://link.aps.org/doi/10.1103/PhysRev.78.695). URL: <https://link.aps.org/doi/10.1103/PhysRev.78.695> (visited on 11/01/2021).
- [27] *Narziss* / *NARZISS* / *Paul Scherrer Institut (PSI)*. URL: <https://www.psi.ch/en/sinq/narziss> (visited on 02/01/2022).
- [28] Julia Katharina Vogel. “Searching for Solar Axions in the eV-Mass Region with the CCD Detector at CAST”. In: (), p. 266.
- [29] Florian M Piegsa et al. “A Ramsey apparatus for the measurement of the incoherent neutron scattering length of the deuteron”. In: *Nuclear Instruments and Methods in Physics Research Section A: Accelerators, Spectrometers, Detectors and Associated Equipment* 589.2 (2008), pp. 318–329.

## Erklärung

gemäss Art. 30 RSL Phil.-nat.18

Name/Vorname: Calic Ivan

Matrikelnummer: 16-103-137

Studiengang: Physics Master, Studienschwerpunkt Experimentalphysik

Bachelor ☐ Master ☒ Dissertation ☐

Titel der Arbeit: Precision magnetometry using Rb-atomic magnetometers and oscillating neutron Ramsey Method: Producing fake axion fields at the NARZISS beamline

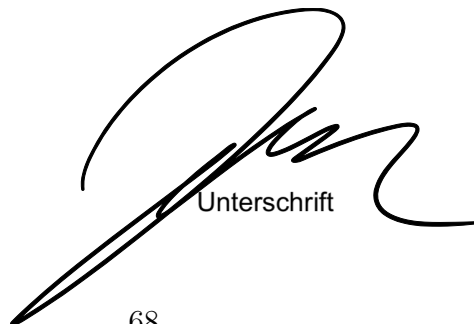
LeiterIn der Arbeit: Prof. Dr. Florian Piegsa

Ich erkläre hiermit, dass ich diese Arbeit selbständig verfasst und keine anderen als die angegebenen Quellen benutzt habe. Alle Stellen, die wörtlich oder sinngemäss aus Quellen entnommen wurden, habe ich als solche gekennzeichnet. Mir ist bekannt, dass andernfalls der Senat gemäss Artikel 36 Absatz 1 Buchstabe r des Gesetzes vom 5. September 1996 über die Universität zum Entzug des auf Grund dieser Arbeit verliehenen Titels berechtigt ist.

Für die Zwecke der Begutachtung und der Überprüfung der Einhaltung der Selbständigkeitserklärung bzw. der Reglemente betreffend Plagiate erteile ich der Universität Bern das Recht, die dazu erforderlichen Personendaten zu bearbeiten und Nutzungshandlungen vorzunehmen, insbesondere die schriftliche Arbeit zu vervielfältigen und dauerhaft in einer Datenbank zu speichern sowie diese zur Überprüfung von Arbeiten Dritter zu verwenden oder hierzu zur Verfügung zu stellen.

Bern, 04.02.2022

Ort/Datum

  
Unterschrift